Chapter 5

Raman Spectroscopy of Spray ILGAR CuInS$_2$ Thin Films

In this chapter, the structural properties of the *well-crystallized top layer* and the *layered bottom layer* (Fig. 3.13) of the Spray ILGAR CuInS$_2$ thin films are studied by Raman Spectroscopy. This was undertaken in order to understand, how each part of the CuInS$_2$ film may influence the photovoltaic performance solar cells, which are based on such films.

The chapter starts with a brief introduction to the theory of Raman spectroscopy and the vibrational properties of CuInS$_2$. The experimental setup used for the Raman measurements is also described (section 5.1.)

After the introductory section, the Raman spectra obtained from the different regions (*well-crystallized top* and *layered bottom layer*) of the Spray ILGAR CuInS$_2$ thin films are investigated in section 5.2.-4. In order to separately probe the *well-crystallized top layer* and the *layered bottom layer*, the films are investigated from the frontside and from the backside. In Fig. 5.1, Raman spectra obtained from both sides of the films are presented. These spectra can be divided into two regions, which show spectral features that relate to the different phases in the films.
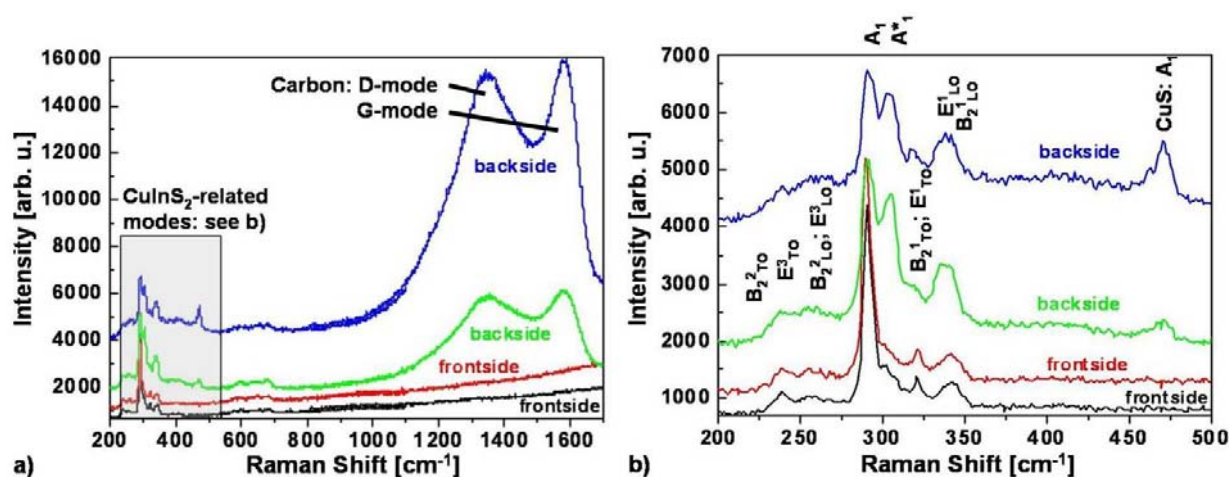

Fig. 5.1:   Raman spectra obtained from two different spots at both the front- and backside of a Spray ILGAR CuInS$_2$ thin film. The Raman modes of chalcopyrite-type and CuAu-ordered (*) CuInS$_2$ are indicated. Additionally, the observed Raman modes of carbon and CuS are labeled. (a) and (b) show the same spectra at different wavenumber ranges. The spectra are shifted on the intensity axis for the sake of clarity.

In the following sections, each phase dominating a specific region of the film is discussed. In section 5.2., the spatial distribution of the two polytypes of CuInS$_2$ (chalcopyrite-type and CuAu-ordered CuInS$_2$) in the film is investigated by Raman spectroscopy. Therefore in

section 5.2., the spectral range of 200-500 cm^{-1} (gray box in Fig. 5.1a; Fig. 5.1b) dominated by the Raman modes of these phases, is analyzed.

In section 5.3., the carbon-containing interlayers in the layered part of the films are investigated by Raman spectroscopy, in order to reveal their composition. Therefore, the carbon D- and G-mode (Fig. 5.1a), which dominate the spectral range between 900 cm^{-1} and 1700 cm^{-1}, are studied.

Finally, in section 5.4., the Raman spectra obtained from the *well-crystallized top layer* of the Spray ILGAR CuInS$_2$ thin films are investigated quantitatively, in order to explain the observed asymmetric spectral shape of the A$_1$ mode of chalcopyrite-type CuInS$_2$. From these investigations, conclusions about the density of crystallographic defects in the *well-crystallized top layer* can be drawn. The latter can be expected to influence the photovoltaic performance of solar cells based on CuInS$_2$ absorber layers.

5.1. Introduction to Raman Spectroscopy

In this section, a brief introduction to Raman spectroscopy and the vibrational properties of CuInS$_2$ is given. Section 5.1.1. describes lattice vibrations in solids in general, whilst in section 5.1.2., the phenomenon of inelastic light scattering in solids is discussed. The symmetry considerations, which lead to the Raman selection rules, are also discussed. In the following, an overview of the vibrational properties of CuInS$_2$ is given in section 5.1.3. At the end of section 5.1., the experimental setup used for the Raman spectroscopy measurements of this thesis is described (section 5.1.4.). Further details about Raman spectroscopy can be found in Ref. [Cardona '82; Kittel '99; Yu '05].

5.1.1. Lattice Vibrations in Solids

The vibration of a crystal lattice leads to displacements of the atoms of the lattice with respect to the position they occupy in rest. These atoms can be considered as oscillators that oscillate with a certain frequency ω. Due to the symmetry of a crystal lattice only vibrations of certain frequencies ω_i can propagate freely through the crystal, i.e., the vibrations are quantized. Each quantum of such lattice vibrations is called a *phonon*. If one formulates the Hamiltonian of a certain crystal lattice, the displacements of the atoms in the crystal can be described by Bloch waves, which depend on the frequency ω and the wave vector $\boldsymbol{q}$. Therefore, the allowed phonons of a certain crystal lattice can be described by a band diagram in reciprocal space in analogy to the electronic band diagram of a semiconductor. In such a diagram each vibrational mode, i.e. each phonon, is described by a phonon dispersion relation $\omega(\boldsymbol{q})$, which assigns a vibration frequency ω to every wave vector $\boldsymbol{q}$. Due to the high degree of symmetry of a crystal lattice, only the oscillations of the atoms of the unit cell have to be considered.

In reciprocal space, the unit cell is represented by the *Brillouin zone*, which is defined as the smallest possible volume enclosed by planes, which are located perpendicular on the centers of reciprocal lattice vectors that have their origin at the Γ-point and is thus located in the center of the Brillouin zone, i.e., at the origin of the reciprocal space. By excitation of phonons with light, i.e., photons of a wavelength λ, only phonons from a very narrow vicinity of the Γ-point can be excited. This is a direct consequence of the rule of momentum conservation. Since the wave vector $\boldsymbol{q}$ of a phonon corresponds to a momentum $\boldsymbol{p} = \hbar\boldsymbol{q}$, an exciting photon of λ = 632.8 nm has an absolute value of the wave vector of $q = 2\pi/\lambda = 9.942 \cdot 10^{-4}$ Å^{-1}. This is about two to three orders of magnitude smaller than the size of the Brillouin zone in typical crystals. Consequently, if in an experiment, phonons are excited in a ideal infinite crystal using light, only such phonons can be detected, which have a non-zero frequency at the Γ-point. Such kind of phonons are called optical phonons, whereas the ones with $\omega(q = 0) \approx 0$ are called acoustic phonons. The acoustic phonons correspond to

traveling sound waves in a solid. The optical phonons, in turn, represent standing waves. For optical phonons, one can distinguish between transverse optical (TO) and longitudinal optical (LO) phonons (analogously for acoustic phonons). For TO phonons, the displacements of the oscillating atoms are perpendicular to the wave vector q, whilst they are parallel to q for LO phonons.

5.1.2. Inelastic Light Scattering by Phonons in Solids

Light traveling through a medium will mainly interact with the medium by transmission, reflection or absorption. These processes follow the standard laws of reflection and refraction [Kittel '99]. Besides these processes, however, a small portion of the light will also be scattered inelastically and thereby its frequency will change [Kittel '99]. This effect is known as "Raman effect" and was predicted by Smekal in 1923 [Smekal '23] and firstly observed by Raman *et al.* in 1928 [Raman '28]. This effect can be explained either by a macroscopic theory or by a microscopic one. Subsequently both theories are briefly described. Thereby, the explanation follows Ref. [Yu '05].

Macroscopic Theory of Raman Scattering

Within the macroscopic theory of Raman scattering, the Raman effect is caused by the dependence of the electronic polarizability of a crystal or a molecule on the displacements of its atoms from their rest position.

In a solid, a periodic electromagnetic field $E = E_0 \cdot \cos(\omega_i \cdot t)$ induces a polarization P:

$$P = \varepsilon_0 \cdot \chi E \qquad \text{Eq. (5.1)}$$

Here, ε_0 is the electric field constant and χ is the tensor of the susceptibility. The periodicity of E leads to a periodicity of P. At a finite temperature, fluctuations in χ are caused by the thermally excited atomic vibrations. The normal modes of such atomic vibrations are quantized into phonons. The atomic displacements Q associated with the phonons can be described as $Q = Q_0 \cdot \cos(\Omega(q) \cdot t)$. Here, the frequency of the phonons depends on the wave vector q. The fluctuations of χ caused by the phonons can be approximated by a Taylor expansion of χ, if $\left| Q \right|$ is much smaller than the lattice constant. For Raman scattering, this condition can be assumed to be fulfilled. The Taylor expansion yields:

$$\chi = \chi_0 + (\partial \chi / \partial Q) \cdot Q + ... \qquad \text{Eq. (5.2)}$$

Substituting Eq. (5.2) into Eq. (5.1) yields an expression, which describes the polarization of the solid in presence of the electromagnetic field:

$$\begin{aligned} P &= \varepsilon_0 \chi_0 E_0 \cdot \cos(\omega_i \cdot t) + \varepsilon_0 (\partial \chi / \partial Q) \cdot Q_0 E_0 \cdot \cos(\Omega(q) \cdot t) \cdot \cos(\omega_i \cdot t) \\ &= \varepsilon_0 \chi_0 E_0 \cdot \cos(\omega_i \cdot t) + 0.5 \cdot \varepsilon_0 (\partial \chi / \partial Q) \cdot Q_0 E_0 \cdot (\cos[(\omega_i - \Omega(q)) \cdot t] + \cos[(\omega_i + \Omega(q)) \cdot t]) \end{aligned} \qquad \text{Eq. (5.3)}$$

In Eq. (5.3), the first term describes the elastically scattered part of the incident electromagnetic field (Rayleigh-scattering), whereas the inelastic scattering is expressed by the second term (Raman-scattering). The latter process leads the emission of photons of the frequencies $\omega_i - \Omega(q)$ and $\omega_i + \Omega(q)$. These photons are referred to as Stokes and Anti-Stokes lines, respectively.

The intensity of the scattered light I_S can be expressed in terms of the susceptibility tensor:

$$I_S = I_I \frac{\omega_S^4 \cdot V'}{(4\pi\varepsilon_0)^2 c^4} \cdot \left| \mathbf{e}_S \underline{\chi} \mathbf{e}_I \right|^2 \qquad \text{Eq. (5.4)}$$

Here, I_I is the intensity of the incident light, ω_S is its frequency, V is the scattering volume, ε is the dielectrical constant of the scattering medium and c is the speed of light. $\mathbf{e}_S$ and $\mathbf{e}_I$, denote the unit vectors of the polarization of the incident and scattered light. If the Taylor expansion of $\underline{\chi}$ (Eq. (5.2)) is substituted into Eq. (5.4), the intensity of the Rayleigh- and Raman-scattered light can be distinguished and the following proportionality is revealed for the intensity of the Raman-scattered light I_{Raman}:

$$I_{Raman} \propto \left| \mathbf{e}_S \frac{\partial \underline{\underline{\chi}}}{\partial \boldsymbol{Q}} \hat{\boldsymbol{Q}}(\Omega(\boldsymbol{q})) \mathbf{e}_I \right|^2 = \left| \mathbf{e}_S \underline{\boldsymbol{R}} \mathbf{e}_I \right|^2 \text{ with } \underline{\boldsymbol{R}} = \frac{\partial \underline{\underline{\chi}}}{\partial \boldsymbol{Q}} \hat{\boldsymbol{Q}}(\Omega(\boldsymbol{q})) \qquad \text{Eq. (5.5)}$$

In Eq. (5.5), $\hat{\boldsymbol{Q}}(\Omega(\boldsymbol{q}))$ is the unit vector of the atomic displacements $\boldsymbol{Q}$. $\underline{\boldsymbol{R}}$ is the so-called Raman tensor, which is a complex second rank tensor[19]. From Eq. (5.5) it can be seen that depending on the Raman tensor the Raman intensity will vanish, if $\mathbf{e}_S$ and $\underline{\boldsymbol{R}}\mathbf{e}_I$ are orthogonal to each other. For which polarization configuration $\mathbf{e}_S$ and $\mathbf{e}_I$ this is the case, follows from the Raman tensor, which is determined by the symmetry of the scattering medium, i.e. the crystal lattice, and of the respective excited vibrational mode, i.e. the phonon and the corresponding periodic atomic displacements. These symmetry requirements, which determine the vanishing of the Raman intensity, are referred to as *Raman selection rules*.

The Raman selection rules for a given crystal lattice can be deduced using group theory [Cardona '82]. Therefore, the space group of the respective lattice has to be identified. This is the group of non-translational symmetry operations of a lattice. In total there are 32 crystallographic point groups, for which the Raman tensors are listed in Ref. [Cardona '82].

Microscopic Theory of Raman Scattering

Analogously to the macroscopic theory, the Raman effect can be explained microscopically on the basis of quantum mechanics [Yu '05]. In this context, the process of Raman scattering is mediated by electrons and can be understood as a sequence of three electronic transitions:

- o Firstly, an incident photon of energy $\hbar\omega_I$ excites an electron from its ground state $|0\rangle$ to an excited state $|a\rangle$. This leads to the creation of an electron-hole pair and the absorption of the photon. Here, $|a\rangle$ can either be a virtual or a real state, if $\hbar\omega_I > E_{gap}$.
- o Subsequently, the excited electron interacts with the lattice of the scattering medium. This leads to the transition of the electron from state $|a\rangle$ to $|a'\rangle$. The energetic difference between the two states is thereby either emitted or absorbed in form of a phonon of energy $\hbar\Omega$.
- o Finally, the electron-hole pair recombines emitting a photon of energy $\hbar\omega_S = \hbar\omega_I - \hbar\Omega$. Thereby, the electron relaxes from the exited state $|a'\rangle$ to its ground state $|0\rangle$.

The transition probability P_{Ph} of the sequence of these three processes for a given phonon can be approximated by third-order perturbation theory as:

$$P_{Ph}(\omega_i) \approx \frac{2\pi}{\hbar} \cdot \left| \frac{\langle 0|\underline{\boldsymbol{H}}_{e-Phot}|a'\rangle \langle a'|\underline{\boldsymbol{H}}_{e-Phon}|a\rangle \langle a|\underline{\boldsymbol{H}}_{e-Phot}|0\rangle}{(E_{a'} - \hbar\omega_s)(E_a - \hbar\omega_i)} + constant \right|^2 \qquad \text{Eq. (5.6)}$$

---

[19] As described in Eq. (5.5) $\underline{\boldsymbol{R}}$ is the Raman tensor for a first order one-phonon process. For higher order processes, Eq.(5.2) needs to be expanded to higher oder terms. Consequently, also $\underline{\boldsymbol{R}}$ will become a tensor of a higher rank.

Here, $\underline{\boldsymbol{H}}_{\text{e-Phot}}$ is the Hamiltonian of the electron-photon interaction, $\underline{\boldsymbol{H}}_{\text{e-Phon}}$ is the Hamiltonian of the electron-phonon interaction and E_a and $E_{a'}$ are the energies of the electronic states $|a\rangle$ and $|a'\rangle$, respectively.

5.1.3. Vibrational Properties of CuInS₂

In this section, the vibrational properties of CuInS₂ are reviewed. The section starts with a brief summary of the deduction of the number of Raman-active modes of CuInS₂. For a more detailed summary of this deduction the reader is referred to Ref. [Rudigier_1 '04] and [Riedle '02]. Previously published work about the observed vibrational modes in chalcopyrite-type and CuAu-ordered CuInS₂ is then reviewed, as a basis for the results presented in the following sections.

The different Raman modes of a given crystal structure can be determined by the *nuclear site group analysis*, which is described in Ref. [Rousseau '81]. Firstly, the space group of the crystal has to be determined, as well as the location of each atom in the unit cell. For the chalcopyrite lattice, the space group is I-42d. In a second step, the *so-called* irreducible representations of the zone-centered phonons (i.e. $q = 0$) must be determined. An irreducible representation constitutes a set of transformation matrices, which represents the symmetry operations of the given structure and thus the lattice itself. These irreducible representations result from the contributions of the non-equivalent, occupied sites in the unit cell of the lattice. They are listed in Ref. [Rousseau '81]. As a last step, the Raman tensors for the irreducible representations, which correspond to Raman-active modes, need to be identified and classified. These tensors can be taken from the tables in Ref. [Cardona '82] for the respective space groups. By nuclear site group analysis the irreducible representation of the chalcopyrite lattice is determined as:

$$\begin{aligned}\Gamma_{\text{chalcopyrite}} &= \underline{\boldsymbol{A}}_1 \oplus 2\underline{\boldsymbol{A}}_2 \oplus \underline{\boldsymbol{B}}_1 \oplus 2\underline{\boldsymbol{B}}_2 \oplus 3\underline{\boldsymbol{E}} \oplus 2\left(\underline{\boldsymbol{B}}_1 \oplus \underline{\boldsymbol{B}}_2 \oplus 2\underline{\boldsymbol{E}}\right) = \\ &= \underline{\boldsymbol{A}}_1 \oplus 2\underline{\boldsymbol{A}}_2 \oplus 3\underline{\boldsymbol{B}}_1 \oplus 4\underline{\boldsymbol{B}}_2 \oplus 7\underline{\boldsymbol{E}}\end{aligned}$$

Eq. (5.7)

From the representations in Eq. (5.7), the $\underline{\boldsymbol{E}}$ representations are doubly degenerate. The corresponding Raman tensors for space group I-42d (chalcopyrite) follow from Ref. [Cardona '82] as:

$$\underline{\boldsymbol{A}}_1 = \begin{pmatrix} a & & \\ & a & \\ & & b \end{pmatrix}; \underline{\boldsymbol{A}}_2 = \begin{pmatrix} & c & \\ -c & & \\ & & \end{pmatrix}; \underline{\boldsymbol{B}}_1 = \begin{pmatrix} d & & \\ & -d & \\ & & \end{pmatrix}; \underline{\boldsymbol{B}}_2 = \begin{pmatrix} & e & \\ e & & \\ & & \end{pmatrix};$$

$$\underline{\boldsymbol{E}}_x = \begin{pmatrix} & & f \\ & & \\ g & & \end{pmatrix}; \underline{\boldsymbol{E}}_y = \begin{pmatrix} & & \\ & & f \\ & g & \end{pmatrix}$$

Eq. (5.8)

For the $\underline{\boldsymbol{E}}$ and $\underline{\boldsymbol{B}}_2$ modes, a LO-TO splitting is observed. Hence, by Eq. (5.7), 28 modes at the zone centers are expressed. This includes optical, as well as acoustic modes. It can be shown that of these modes, two are acoustic modes ($1\underline{\boldsymbol{B}}_2 \oplus 1\underline{\boldsymbol{E}}$). Thus, for chalcopyrite-type CuInS₂, 24 optical modes exist. Except the $\underline{\boldsymbol{A}}_2$ modes, which are inactive, all of these are Raman-active. This leads to the prediction of 22 optical Raman-active modes that should observable in Raman measurements of chalcopyrite-type CuInS₂[20].

---

[20] For the sake of simplicity, in the following the Raman-modes will be written as constants (X) instead of the tensor form in Eq. (5.8) ($\underline{X}$).

Numerous reports exist about the phonon modes in chalcopyrite-type CuInS$_2$ [Koschel '75; Koschel_1 '75; Neumann '84; Neumann '85; Ohrendorf_1 '99; Ohrendorf_2 '99; Ohrendorf_3 '99]. Of the 22 optical Raman modes predicted for chalcopyrite-type CuInS$_2$, all but three modes have been measured by Koschel *et al.* using infrared (IR) and Raman spectroscopy [Koschel '75; Koschel_1 '75]. However, in polycrystalline CuInS$_2$ thin films, Rudigier only found 9 of these modes using Raman spectroscopy [Rudigier_1 '04]. The same modes were also observed in the present work at similar positions. In Table 5.1 the experimentally determined modes are listed.

Table 5.1:   Predicted and experimentally observed lattice vibrations as measured by Koschel *et al.* by IR and Raman spectroscopy at single crystalline CuInS$_2$ [Koschel '75; Koschel_1 '75] and by Rudigier by Raman spectroscopy at CuInS$_2$ thin films [Rudigier_1 '04] and in the course of this work

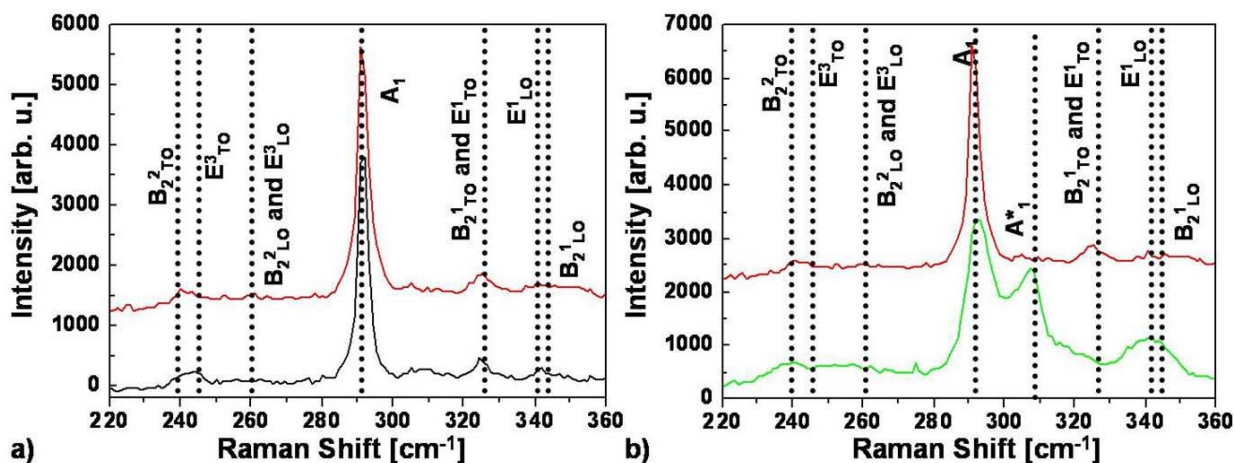| Predicted mode	Raman shift [cm^{-1}] [Koschel '75; Koschel_1 '75]	Raman shift [cm^{-1}] [Rudigier_1 '04]	Raman shift [cm^{-1}] this work	Predicted mode	Raman shift [cm^{-1}] [Koschel '75; Koschel_1 '75]	Raman shift [cm^{-1}] [Rudigier_1 '04]	Raman shift [cm^{-1}] this work
A_1	294	290	292	E^2_{TO}	295	/	/
B_1^1	/	/	/	E^3_{TO}	244	240	244
B_1^2	/	/	/	E^4_{TO}	140	/	/
B_1^3	/	/	/	E^5_{TO}	88	/	/
$B_2^1{}_{TO}$	323	323	326	E^6_{TO}	67	/	/
$B_2^2{}_{TO}$	234	237	240	E^1_{LO}	339	338	341
$B_2^3{}_{TO}$	79	/	/	E^2_{LO}	314	/	/
$B_2^1{}_{LO}$	352	345	344	E^3_{LO}	260	259	260
$B_2^2{}_{LO}$	266	259	260	E^4_{LO}	140	/	/
$B_2^3{}_{LO}$	79	/	/	E^5_{LO}	88	/	/
E^1_{TO}	321	323	326	E^6_{LO}	67	/	/

Fig. 5.2:   a) CuInS$_2$ Raman spectra measured in the course of this work; the red upper spectrum was measured at a CuInS$_2$ thin film, the black lower spectrum was measured at a single crystal. b) Raman spectra of a single phase chalcopyrite-type CuInS$_2$ thin film (red upper spectrum) and of a CuInS$_2$ thin film that contains CuAu-ordered CuInS$_2$ as a secondary phase (green lower curve); the asterisk* marks the only detected mode of CuAu-ordered CuInS$_2$ (A*$_1$). The spectra are shifted on the intensity axis for the sake of clarity.

In Fig. 5.2a, two CuInS$_2$ Raman spectra are shown, which were measured during the present work. The red spectrum was measured on a single crystal and the black one on a thin film, as was used by Rudigier.

As mentioned in section 2.1.2, besides chalcopyrite-type CuInS$_2$ also CuAu-ordered CuInS$_2$ has been observed by various authors [Su '98; Alvarez-Garcia '02; Alvarez-Garcia '05]. It has been shown that in this material an additional vibrational mode at about 305 cm^{-1} could be observed by Raman spectroscopy. This mode was assigned to the A$_1$ mode of CuAu-ordered CuInS$_2$ [Alvarez-Garcia '02; Riedle '02]. In Fig. 5.2b, the Raman spectrum of a CuInS$_2$ thin film is shown, which contains CuAu-ordered CuInS$_2$ as a secondary phase. The frequencies of the optical phonon modes for CuAu-ordered CuInS$_2$ were calculated by Fritsch and Riedle by density functional theory [Riedle '02]. The obtained Raman shifts are listed in Table 5.2.

Table 5.2:   Calculated Raman shifts for the optical phonons of CuAu-ordered CuInS$_2$ as calculated in Ref. [Riedle '02]

Mode	Frequency [cm^{-1}]
A$_1$	305
B$_2^1$	287
B$_2^2$	145
E^1	299
E^2	236
E^3	69

From these calculated frequencies only the A$_1$ mode could be identified unambiguously by Riedle [Riedle '02]. Another mode was observed at 60 cm^{-1}, which possibly may be assigned to the E^3 mode [Riedle '02].

5.1.4. Experimental Setup

For the Raman measurements a DILOR LabRAM Micro-Raman spectrometer in backscattering configuration, equipped with an optical Olympus microscope and a moveable xy-table, on which the sample was mounted, was used. A HeNe laser (λ = 632.8 nm; 2.5 mW) was used for excitation. The optical setup of the Raman spectrometer is sketched in Fig. 5.3.
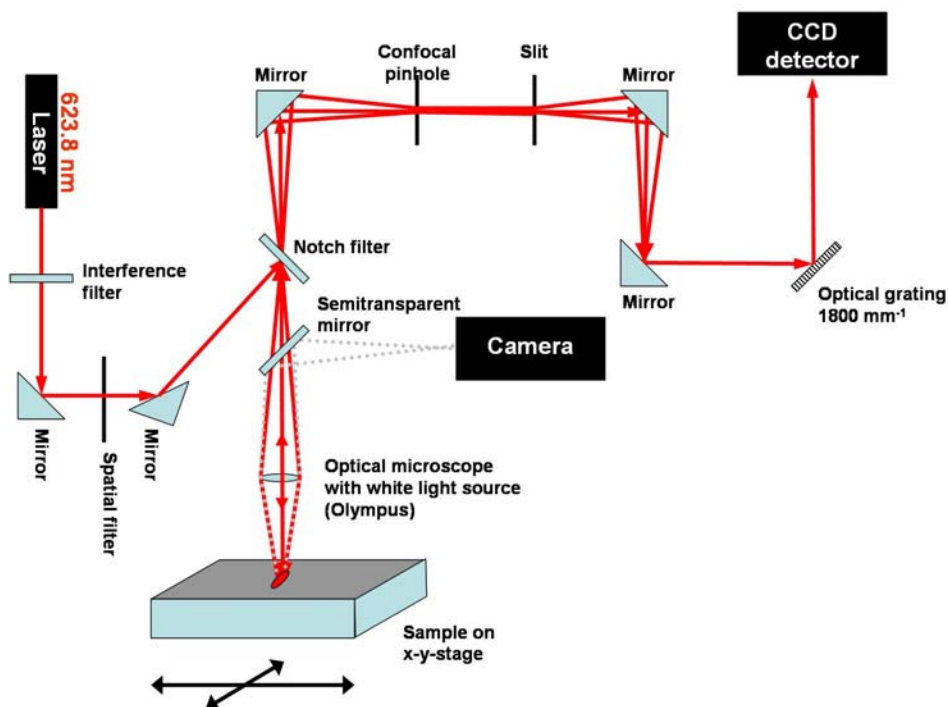

Fig. 5.3:   Optical setup of a DILOR LabRAM Micro-Raman spectrometer equipped with an Olympus optical microscope.

The laser beam was focused onto the sample by the microscope lens. Thus, the diameter of the laser spot could be varied between 1-2 µm and 1 mm. If not stated otherwise, all following Raman spectra were recorded using the minimum spot size of 1-2 µm (micro-Raman). The microscope could also be used to image the film surface for the probed region. In order to prevent the film damage, the intensity of the laser beam was filtered by an interference filter by a factor of 10 (250 µW). The Rayleigh-scattered light was excluded from the detected backscattered light by applying a notch filter. The Raman shifts were detected by a 1800 mm^{-1} grating focused on a CCD camera.

The duration of the Raman measurements varied between 120 s and 240 s per spectra, depending on the requirements of the signal-to-noise ratio. The penetration depth of the laser light of about 150 nm was calculated by using the absorption coefficient of chalcopyrite-type CuInS$_2$ from Ref. [Neumann '81].

For comparative measurements of the relative contributions of the A$_1$ modes of chalcopyrite-type and CuAu-ordered CuInS$_2$, a spectral resolution of ± 1 cm^{-1} was sufficient. The same was true for the comparison of the D- and G-modes of carbon. Therefore, the Raman spectrometer was calibrated using the 520.7 cm^{-1} first-order Raman spectrum of a silicon wafer [Parker '67], after a heating period of the laser of 30 min, which allowed it to reach thermal equilibrium. For this procedure the thermal shift of the laser line during the rest of the day was in the range of 0.3 cm^{-1} and thus below the desired resolution. This calibration procedure was applied for the measurements presented in sections 5.2 and 5.3. However, for the precise strain determination needed for fitting the spectral shape of the A$_1$ mode of chalcopyrite type CuInS$_2$ in section 5.4., a higher accuracy was needed. In the following, the calibration procedure applied for these measurements is described.

Calibration Procedure for Strain Determination

The Raman spectra of section 5.4. were all recorded under identical conditions (240 s per spectra; laser spot diameter 1-2 µm). In order to account for the shift of the laser energy due to heating of the setup, the first order Raman spectrum of a silicon wafer was recorded before and after every CuInS$_2$ spectrum. The line positions of these spectra were determined from these spectra by fitting them with a standard Lorentzian [Yu '05] and are shown in Fig. 5.4. as a function of the time of measurements.
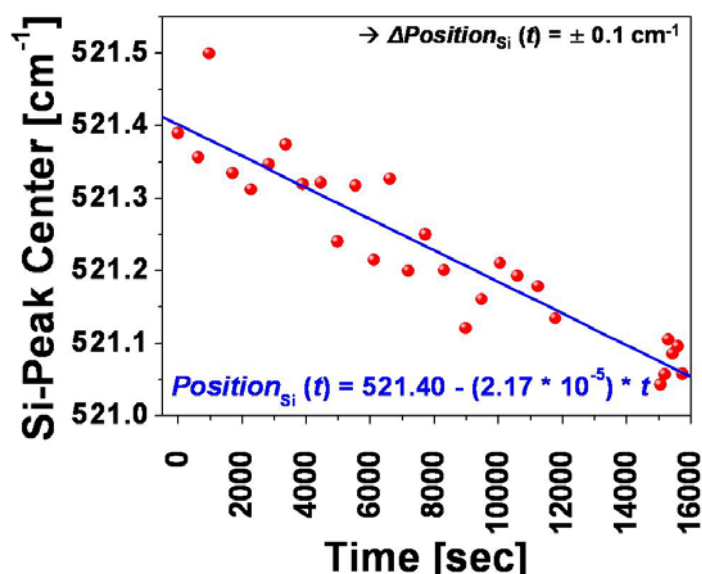

Fig. 5.4: Thermal shift of the first order Raman peak position (●) of a silicon wafer that was used for calibrating the Raman spectrometer. The blue line is a linear fit of the data. All Raman spectra have been corrected to a Si-peak position of 520.7 cm-1 [Parker '67]. From the scattering of the Si-peak positions around the linear fit, the uncertainty of the measured was determined as ± 0.1 cm^{-1}.

Inside figure:
$\rightarrow \Delta Position_{Si}(t) = \pm\,0.1$ cm^{-1}

$Position_{Si}(t) = 521.40 - (2.17 * 10^{-5}) * t$

Axis labels: Si-Peak Center [cm^{-1}]; Time [sec]

The Si-peak position shifts linearly with time. Therefore, this shift of the laser line was compensated for by correcting all CuInS$_2$ spectra to a Si-peak position of 520.7 cm^{-1} [Parker

'67]. It can also be seen from Fig. 5.4 that the peak positions scatter around the linear fit with a maximum deviation of $\Delta Position_{Si} = 0.1$ cm^{-1}. This deviation determines the accuracy of the measurements and thus also the uncertainties of the strains obtained from the spectra.

5.2. CuAu-Order and Secondary Phases in Spray ILGAR CuInS$_2$ Thin Films

In this section, the spatial distribution of CuAu-ordered CuInS$_2$ (see section 2.1.2.) in Spray ILGAR CuInS$_2$ thin films is investigated, which were prepared as described in section 3.3.2. Álvarez-García *et al.* [Alvarez-Garcia_1 '03; Rudigier '04] showed that the presence of CuAu-ordered CuInS$_2$ in RTP-processed CuInS$_2$ absorber layers causes a degradation of the solar cells based on these absorbers. Therefore, the presence of CuAu-ordered CuInS$_2$ is anticipated to affect the photovoltaic performance of Spray ILGAR CuInS$_2$-based solar cells.
As a basis for these investigations, the section starts with a discussion of the influence of secondary binary and ternary indium and copper phases on the Raman spectrum of Spray ILGAR CuInS$_2$ thin films (section 5.2.1.).
Afterwards, the distribution of CuAu-ordered CuInS$_2$ in *as-deposited* Spray ILGAR CuInS$_2$ thin films is investigated (section 5.2.2.), whilst its distribution in *H$_2$S and KCN treated* Spray ILGAR CuInS$_2$ thin films is studied subsequently (section 5.2.3.). Furthermore, the spatial distribution of CuAu-ordered CuInS$_2$ is correlated to the distribution of other secondary phases (In$_2$O$_3$, Cu$_{2-x}$S ($0 \leq x \leq 0.2$)) present in the Spray ILGAR CuInS$_2$ thin films.

5.2.1. Influences of Secondary Phases on the CuInS$_2$ Raman Spectrum

The as-deposited Spray ILGAR CuInS$_2$ thin films consist of thin layers (about 30 nm each) containing CuInS$_2$ and In$_2$O$_3$. These layers are separated by interlayers of a yet unidentified carbon-containing phase. On top of the films, Cu$_{2-x}$S agglomerates were observed (Fig. 4.19). In this section, Micro-Raman spectroscopy is applied to correlate the spatial distribution of CuAu-ordered and chalcopyrite-type CuInS$_2$ to the distribution of these secondary phases. Thereby, the contributions of Cu$_{2-x}$S, In$_2$O$_3$ and of the carbon-containing interlayers to the Raman spectrum have to be distinguished from those of both CuInS$_2$ phases. Therefore, the influence of the secondary phases on the Raman spectra of chalcopyrite-type and CuAu-ordered CuInS$_2$ is assessed in the following.
It will be shown in section 5.3. that the carbon-containing interlayers do not contribute to the spectrum in the wavenumber region discussed in the present section (200-500 cm^{-1}). Therefore, this phase is not considered for the remainder of this section.
The Raman modes of In$_2$O$_3$ and Cu$_{2-x}$S ($0 \leq x \leq 0.2$) for wavenumbers of 200-500 cm^{-1} are listed in Table 5.3. Even though only In$_2$O$_3$ and Cu$_{2-x}$S were detected as secondary phases in the Spray ILGAR CuInS$_2$ thin films, the presence of Cu$_{2-x}$S ($x > 0.2$), CuIn$_5$S$_8$, In$_2$S$_3$ and InS, could not be excluded according to the growth model deduced in chapter 4. Consequently, the Raman modes of these phases are also included in Table 5.3.
The comparison of the Raman modes listed in Table 5.3 with those of chalcopyrite-type (Table 5.1) and CuAu-ordered CuInS$_2$ (Table 5.2) shows that no Raman lines of any copper sulfide phases (Cu$_{2-x}$S; $0 \leq x \leq 2$) are observed in the wavenumbers range 290-350 cm^{-1}, in which the most intense modes of chalcopyrite-type and CuAu-ordered CuInS$_2$ are found (Fig 5.2). Hence, these phases will not influence the Raman modes of either CuInS$_2$ phases.
For InS, one mode (315 cm^{-1}) is observed in the relevant wavenumber range of 290-350 cm^{-1}. However, the most intense mode of InS between 200-500 cm^{-1} is observed at 215 cm^{-1}, where no modes of chalcopyrite-type or CuAu-ordered CuInS$_2$ are found. Thus, the presence of InS would be indicated by the 215 cm^{-1} mode and could be taken into account for the interpretation of the Raman spectra. The same is true for β- and α-In$_2$S$_3$, which also exhibit Raman modes in the range 290-350 cm^{-1}, but have their most intense mode at 266 cm^{-1}.

For CuIn$_5$S$_8$ and In$_2$O$_3$, the most intense Raman modes are observed at 349 cm^{-1} and 306 cm^{-1}, respectively. Therefore, they may influence the Raman spectra of chalcopyrite-type or CuAu-ordered CuInS$_2$ without being noticed. Therefore, their influence is assessed subsequently.

Table 5.3:   Reported and measured Raman modes of CuIn$_5$S$_8$, InS, α-In$_2$S$_3$, β-In$_2$S$_3$, CuS, Cu$_{2-x}$S (0≤x≤0.2), In$_2$O$_3$ in the wavenumber range of 200-500 cm^{-1} that is relevant for the analysis in this section. The modes for chalcopyrite-type and CuAu-ordered CuInS$_2$ are given in Tables 5.1 and 5.2, respectively. The abbreviation "n. a." Stands for not assigned. The asterisk * marks the mode of maximum intensity in the wavenumber range of 200-500 cm^{-1}.

Phase	Peak center [cm^{-1}]	Symmetry	References
Chalcopyrite-type CuInS$_2$	*See Table 5.1*		
CuAu-ordered CuInS$_2$	*See Table 5.2*		
CuIn$_5$S$_8$	258; 262	$F_{1\,LO}^{2}$	This work; [Gasanly '93]
	304; 308	F_2^2	
	349; 350*	F_2^3	
	359; 362	A_1	
InS	215*	n. a.	[Rudigier_1 '04]
	260	n. a.	
	315	n. a.	
α -In$_2$S$_3$	245; 246	n. a.	This work; [Kambas '81]
	265; 266*	n. a.	
	307; 306	n. a.	
	325; 326	n. a.	
	366; 365	n. a.	
β-In$_2$S$_3$	As β-In$_2$S$_3$	n. a.	[Kambas '81]
CuS	262; 267; 267	n. a.	This work; [Ishii '93]; [Riedle '02]
	470*; 474; 475	A_1	
Cu$_x$S$_y$ (x<y)	418	n. a.	[Munce '07]
	424	n. a.	
	422	n. a.	
	469*	A_1	
Cu$_{2-x}$S (0.6≤x≤1)	265-270	n. a.	
	474*	A_1	
Cu$_{2-x}$S (0≤x<0.6)	inactive	n. a.	
In$_2$O$_3$	306; 308*	n. a.	This work; [Korotcenkov '07]
	365; 365	n. a.	
	/; 471	n. a.	
	495; 504	n. a.	

Raman spectra obtained from a CVT-grown CuIn$_5$S$_8$ polycrystal and from In$_2$O$_3$ powder (Chempur™) are shown in Fig. 5.5.
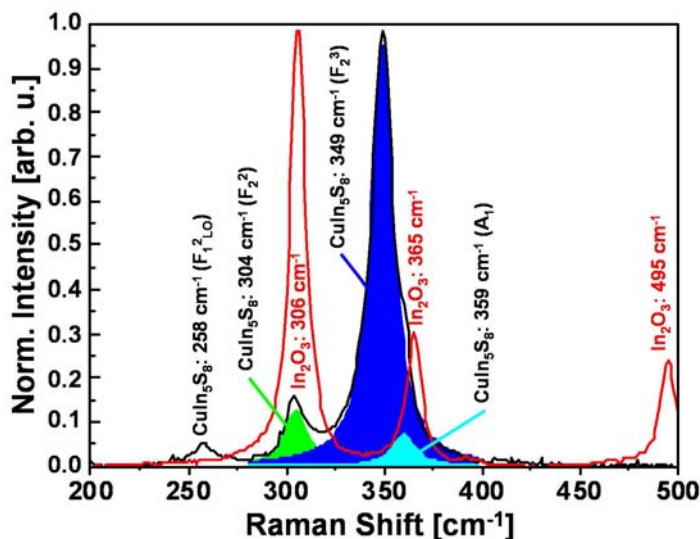

Fig. 5.5:   Raman spectra obtained from a CVT-grown CuIn$_5$S$_8$ polycrystal (black line) and from In$_2$O$_3$ powder (Chempur™) (red line). The Raman modes are indicated according to Table 5.3. For CuIn$_5$S$_8$, overlapping modes have been fitted by Lorentzian contributions, which are also shown in Fig. 5.5.

The measured spectra matched well with spectra for CuIn$_5$S$_8$ and cubic In$_2$O$_3$ reported by other authors [Gasanly '93; Korotcenkov '07]. The most intense CuIn$_5$S$_8$ (F$_2^3$) mode is located at 349 cm^{-1} and its intensity exceeds that of the F$_2^2$ mode (304 cm^{-1}), which coincides with the A$_1$ mode of CuAu-ordered CuInS$_2$ (305 cm^{-1}) by a factor of about seven. Therefore, a possible influence of the CuIn$_5$S$_8$ F$_2^2$ mode on the A$_1$ mode of CuAu-ordered CuInS$_2$ (305 cm^{-1}) is negligible, *if* no intense CuIn$_5$S$_8$ F$_2^3$ mode is observed at 349 cm^{-1}.

Finally, the influence of the In$_2$O$_3$ Raman mode at 306 cm^{-1} on the A$_1$ mode of CuAu-ordered CuInS$_2$ (305 cm^{-1}) is considered. This influence is especially critical for two reasons:

- o Firstly, the mode at 306 cm^{-1} is the most intense In$_2$O$_3$ mode and thus its contribution to the spectrum may not necessarily be revealed by the contribution of other modes.
- o Secondly, In$_2$O$_3$ is known to be present in the as-deposited Spray ILGAR CuInS$_2$ thin films (up to 25 mol. %; Fig. 4.12). Hence, its contribution cannot be excluded by complimentary methods.

In order to assess the influence of the In$_2$O$_3$ content on the Raman spectrum of as-deposited Spray ILGAR CuInS$_2$ thin films, the absolute Raman scattering intensities obtained from an In$_2$O$_3$-free Spray ILGAR CuInS$_2$ thin film were compared to those obtained from a 1 μm thick In$_2$O$_3$ thin film grown epitaxially on a sapphire substrate. The Raman spectra obtained from both samples are shown in Fig. 5.6.
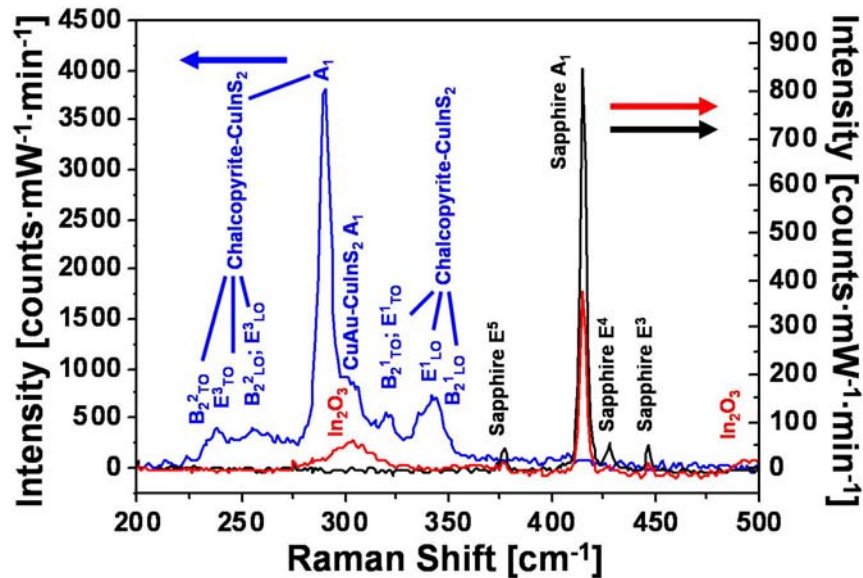

Fig. 5.6:   Comparison of the absolute Raman intensity obtained from a Spray ILGAR CuInS$_2$ thin film (blue curve; sample 421; Fig. 4.18e, f) and a 1μm thick epitaxial In$_2$O$_3$ thin film deposited onto a sapphire substrate (red curve). For comparison also the spectrum obtained from the plain sapphire substrate is shown (black curve). For In$_2$O$_3$ no assignment of the Raman modes is reported (Table 5.3). The sapphire modes were assigned according to Ref. [Watson '81].

The absolute Raman intensity of the In$_2$O$_3$ Raman mode at 306 cm^{-1} obtained from the In$_2$O$_3$ film is about 50 counts·mW^{-1}·min^{-1}, whilst the Raman intensities obtained for the A$_1$ modes of chalcopyrite-type and CuAu-ordered CuInS$_2$ are about 4000 counts·mW^{-1}·min^{-1} and 925 counts·mW^{-1}·min^{-1}, respectively. In the following, only relative changes of the intensities of the A$_1$ modes of chalcopyrite-type and CuAu-ordered CuInS$_2$ are considered. It is assumed that the contribution of In$_2$O$_3$ to the Raman spectrum of Spray ILGAR CuInS$_2$ can be neglected due to the low Raman scattering intensity of In$_2$O$_3$. The latter is likely due to the large band gaps of In$_2$O$_3$ of E_{gap} = 2.1-2.7 eV (indirect) and E_{gap} = 3.6 eV (direct) [Hamberg '86; Klein '00; Erhart '07]. These band gaps are larger than the energy of the exciting laser (633 nm = 1.96 eV), whereas the band gaps of both CuInS$_2$ phases are lower: The band gap of chalcopyrite-type CuInS$_2$ was determined as E_{gap} = 1.5 eV (direct) [Neumann '81] and for

CuAu-ordered CuInS$_2$, the band gap was calculated to be reduced by $\Delta E_{gap} = 0.03$ eV [Wei '99]. Therefore, both CuInS$_2$ phases strongly absorb the exciting laser light in Raman measurements (compare Fig. 6.9b), whereas In$_2$O$_3$ is transmitted and can only interact with the exciting photons via virtual states (see section 5.1.2).

In conclusion, the considerations about the influence of secondary phases on the Raman spectra of Spray ILGAR CuInS$_2$ thin films show that the intensity ratio of the A$_1$ modes of chalcopyrite-type and CuAu-ordered CuInS$_2$ is not significant, *provided* no modes of CuIn$_5$S$_8$, InS or β- and α-In$_2$S$_3$, are observed at wavenumbers of 349 cm^{-1}, 215 cm^{-1} and 266 cm^{-1}, respectively. The Raman modes of Cu$_{2-x}$S ($0 \leq x \leq 2$) and In$_2$O$_3$ do not influence the intensity ratio of the A$_1$ modes of chalcopyrite-type and CuAu-ordered CuInS$_2$ in any case.

5.2.2. Raman Spectroscopy of As-Deposited Spray ILGAR CuInS$_2$ Thin Films

In section 4.4.2.2., it was shown that after removing the Cu$_{2-x}$S agglomerates by KCN, the film surface exhibited two different morphologies and compositions (Fig. 4.15). One region, referred to as "*homogeneous*" in the following, showed a homogeneous morphology with grain sizes below 100 nm. This region was found to be indium- and oxygen-rich. The other region, referred to as "*inhomogeneous*" in the following, consisted of grains of diameters of several hundred nanometers and was copper- and sulfur-rich. In section 4.4.2.3., it was shown that the Cu$_{2-x}$S agglomerates are located on top of the inhomogeneous regions. These two regions were observed for all as-deposited Spray ILGAR CuInS$_2$ thin films, independently of their precise preparation parameters. The latter solely influenced the spatial distribution of both regions. In Fig. 5.7, two plan-view optical micrographs of Spray ILGAR CuInS$_2$ thin films are shown, on which the homogeneous and inhomogeneous regions are indicated.
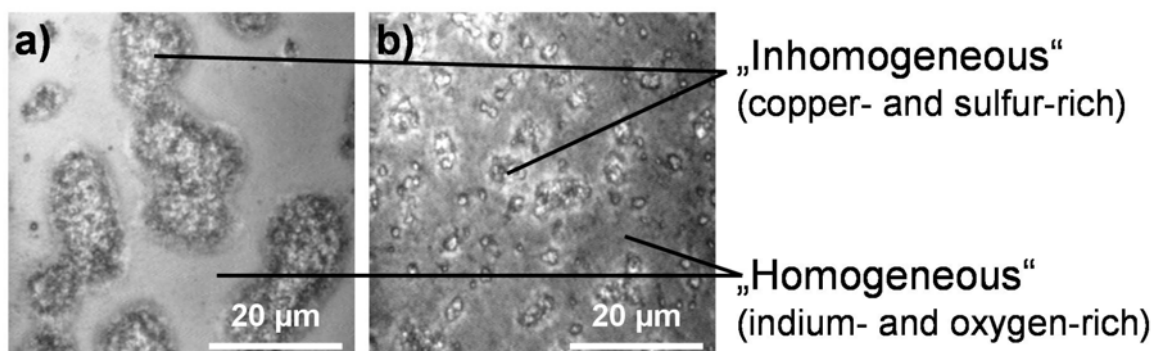

Fig. 5.7:   Surface morphology of as-deposited Spray ILGAR CuInS$_2$ thin films: Plan-view optical micrographs of the surface of as-deposited Spray ILGAR CuInS$_2$ thin films (samples 418 (a) and 329 (b)), which were prepared using spraying solutions of different [Cu]:[In] ratios (a: 1.25; b: 1) and different H$_2$S step durations in the ILGAR-cycle (a: 60 s; b: 20 s). These preparation parameters constitute two extremes of the covered parameter window. Independently of the preparation parameters, the surface consists of a "*homogeneous*" and an "*inhomogeneous*" region. It was shown (Fig. 4.15) that the homogeneous region is indium- and oxygen-rich, whilst the inhomogeneous region is copper- and sulfur-rich. The detailed preparation parameters are listed in Appendix I.

In the following, the spatial distribution of the chalcopyrite-type and CuAu-ordered phase is correlated to the distribution of the homogeneous and inhomogeneous regions of the films.

In Fig. 5.8, typical Raman spectra obtained from an as-deposited Spray ILGAR CuInS$_2$ thin film (*no KCN etching*) are shown. Of these, the red and black spectra were recorded on the inhomogeneous regions of the films, while the cyan, blue and green spectra were recorded on the homogeneous regions. From the comparison of these spectra to the spectra of single phase chalcopyrite-type CuInS$_2$ thin films (Fig. 5.2a), several observations can be made, which will be discussed in detail afterwards:
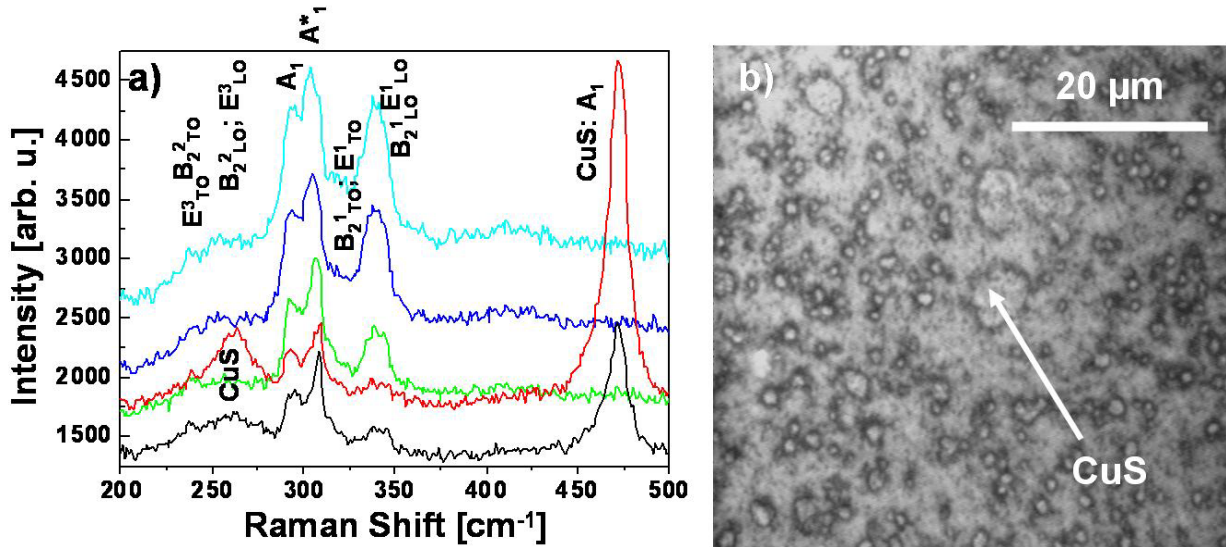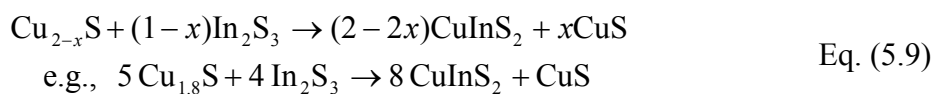
Fig. 5.8: Raman spectra measured at five different spots (a) and optical micrograph (b) of an as-deposited Spray ILGAR CuInS$_2$ thin film (sample329). The red and black spectra were recorded on the inhomogeneous regions of the films, while the cyan, blue and green spectra were recorded on the homogeneous regions. The spectra are shifted o the intensity axis for the sake of clarity. The Raman modes of chalcopyrite-type CuInS$_2$ are indicated in a). The A$_1$ mode of CuAu-ordered CuInS$_2$ is marked by an asterisk *. The CuS modes are also indicated. The diameter of the exciting laser spot was about 1-2μm. The arrow in b) marks a spot, at which CuS was detected by Raman Spectroscopy.

- Two modes, which can be assigned to Cu$_{2-x}$S phases with 0.6≤x≤1 (262 cm^{-1}; 470 cm^{-1} (A$_1$); Table 5.3), were observed in the spectra recorded on the inhomogeneous regions (Fig. 5.8b). In order to avoid confusions with Cu$_{2-x}$S phases with 0≤x≤0.2, the copper-rich phases with 0.6≤x≤1 are summarized as CuS in the following. In contrast, no copper sulfide phases were observed on the homogeneous regions.
- The intensity of the A$_1$ mode of CuAu-ordered CuInS$_2$ (305 cm^{-1}; A$_1$*) exceeds that of the A$_1$ mode of chalcopyrite-type CuInS$_2$ (292 cm^{-1}; A$_1$) in all recorded spectra.
- A variation of the relative intensity of the Raman mode centered at 340 cm^{-1}, which can be assigned to the superimposed E$^1_{LO}$ (341 cm^{-1}) and B$_2^1_{LO}$ (344 cm^{-1}) modes of chalcopyrite-type CuInS$_2$, compared to the intensities of the A$_1$ modes of both CuInS$_2$ phases can be observed. In particular the relative intensity of the superimposed E$^1_{LO}$ and B$_2^1_{LO}$ modes exceeds that observed in single-phase chalcopyrite-type samples.

CuS Raman Modes in Raman Spectra of As-Deposited Spray ILGAR CuInS$_2$ Thin Films

The presence of CuS in the as-deposited Spray ILGAR CuInS$_2$ thin films in Fig. 5.8 can be assumed to result from the CuInS$_2$ formation process, since no CuS has been observed by XRD[21] in the Spray ILGAR Cu$_{2-x}$S (0≤x≤0.2) thin films investigated in section 3.1.4. If CuInS$_2$ is formed by the reaction of In$_2$S$_3$ with a Cu$_{2-x}$S compound with 0≤x≤0.2, the reaction can be described as:

$$Cu_{2-x}S + (1-x)In_2S_3 \rightarrow (2-2x)CuInS_2 + xCuS$$
$$\text{e.g., } 5\,Cu_{1.8}S + 4\,In_2S_3 \rightarrow 8\,CuInS_2 + CuS$$

Eq. (5.9)

---

[21] Also by Raman spectroscopy, no evidence was found for the presence of CuS in Spray ILGAR Cu$_{2-x}$S thin films. No Raman-active phase was observed in these films, which indicates that x<0.6 (Table 5.3) and agrees well with the phases observed by XRD (α-Cu$_2$S, Cu$_{1.81}$S and Cu$_9$S$_5$) in Fig. 3.5.

Therefore, it is likely that all detected CuS has been formed during the formation of CuInS$_2$. In contrast to CuS, Cu$_{2-x}$S compounds with $x<0.6$ are Raman-inactive (Table 5.3; [Riedle '02; Munce '07]). However, note that the CuS modes at 262 cm^{-1} and 470 cm^{-1} were only observed in some Raman spectra obtained from the inhomogeneous regions of as-deposited Spray ILGAR CuInS$_2$ thin films, while in other spectra recorded on the same films, no copper sulfide-related Raman modes were observed. Thus it maybe assumed that the Raman-inactive Cu$_{2-x}$S phases are the dominating copper sulfide phases in the as-deposited Spray ILGAR CuInS$_2$ thin films and that CuS is only formed locally. This agrees well with observations of Riedle [Riedle '02], who observed by Raman Spectroscopy and XRD that for CuInS$_2$ thin films prepared from metallic precursors by H$_2$S annealing the segregated Cu$_{2-x}$S mainly consists of Raman-inactive Cu$_9$S$_5$ with only minor amounts CuS.

CuAu-ordered CuInS$_2$ in As-Deposited Spray ILGAR CuInS$_2$ Thin Films

In order to investigate the spatial distribution of the CuAu-ordered CuInS$_2$ phase in the Spray ILGAR CuInS$_2$ thin films, Raman spectra were recorded on the inhomogeneous and homogeneous regions of nine different as-deposited Spray ILGAR CuInS$_2$ thin films that were already characterized in section 4.4. (samples 329,330, 412-418; Table 4.2) and covered a wide parameter window of [Cu]:[In] ratios ($1 \leq$ [Cu]:[In] ≤ 2) and H$_2$S step durations in the ILGAR-cycle (20 s $\leq \Delta t_{H_2S} \leq$ 120s) (Appendix I). In order to exclude damping effects of the copper sulfide agglomerates, these were removed by KCN etching of the samples. As in the Raman spectra shown in 5.8a, the intensity of the A$_1$ mode of CuAu-ordered CuInS$_2$ exceeded the intensity of the A$_1$ mode of chalcopyrite-type CuInS$_2$ in all recorded Raman spectra, no matter if they were recorded on the homogeneous or inhomogeneous regions of the films.

In the following, the contributions of the A$_1$ modes of CuAu-ordered and chalcopyrite-type CuInS$_2$ to the Raman spectra obtained from the homogeneous and inhomogeneous regions of the films are evaluated quantitatively. Therefore, the peak area ratio of the A$_1$ modes of chalcopyrite-type and CuAu-ordered CuInS$_2$ was determined by fitting the Raman spectra by Lorentzian contributions in the wavenumber range of 260-400 cm^{-1}. Due to the overlap of the numerous modes in this spectral range (A$_1$ (292 cm^{-1}), B$_2^1{}_{TO}$+E$^1{}_{LO}$ (326 cm^{-1}), B$_2^1{}_{LO}$ (344 cm^{-1}), B$_2^2{}_{LO}$+E$^3{}_{LO}$ (260 cm^{-1}), E$^1{}_{LO}$ (340 cm^{-1}) for chalcopyrite-type CuInS$_2$ and A$_1$ (305 cm^{-1}) for CuAu-ordered CuInS$_2$; Table 5.1 and 5.2), not all modes could be resolved by the fits. Therefore, the spectra were fitted by only three Lorentzians, which accounted for the main peaks observed in the spectra: one for each A$_1$ mode and another one that accounted for the superimposed E$^1{}_{LO}$ and B$_2^1{}_{LO}$ modes. By applying this procedure, all spectra could be fitted well and the comparability between the fitted spectra was ensured. In Fig. 5.9, two fits of typical spectra obtained from the homogeneous (a) and inhomogeneous (b) region of an as-deposited Spray ILGAR CuInS$_2$ thin film are shown. Both spectra can be well described by the contributions of the A$_1$ modes of chalcopyrite-type and CuAu-ordered CuInS$_2$ centered at 292 $\pm$ 1 cm^{-1} and 305 $\pm$ 1 cm^{-1} and another peak at 338 $\pm$ 1 cm^{-1} accounting for the superimposed E$^1{}_{LO}$ and B$_2^1{}_{LO}$ modes. These positions match well to those listed in Tables 5.1 and 5.2 for the respective modes indicating that the contribution of other modes is negligible.

Note that the peak area ratios are not corrected for the Raman cross-sections of chalcopyrite-type CuInS$_2$ and CuAu-ordered CuInS$_2$. Since no single-phase samples of the metastable CuAu-ordered CuInS$_2$ (section 2.1.2.) exist, the absolute Raman scattering intensities of chalcopyrite-type CuInS$_2$ and CuAu-ordered CuInS$_2$, could not be determined independently from each other. Thus, in the following discussion only relative changes in the peak area ratio are considered for investigating the spatial distribution of CuAu-ordered CuInS$_2$ in the as-deposited Spray ILGAR CuInS$_2$ thin films, which do not necessarily reflect the compositional ratio of both CuInS$_2$ phases.
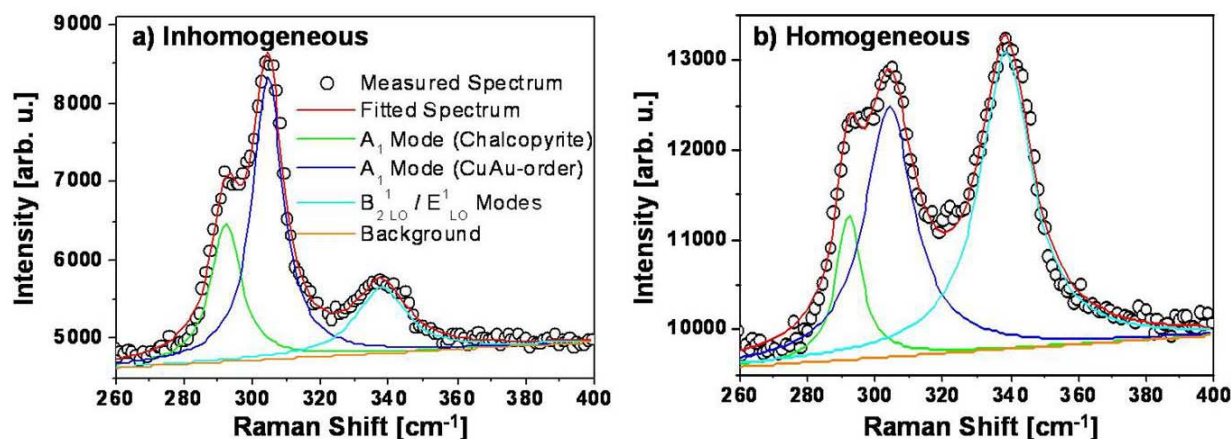
Fig. 5.9:   Examples of measured Raman spectra obtained from the inhomogeneous (copper- and sulfur-rich, (b)) and homogeneous (indium- and oxygen-rich, (b)) regions of an as-deposited Spray ILGAR CuInS$_2$ thin film (sample 415; Appendix I). The Raman spectra were fitted with Lorentzian contributions in order to obtain the peak area ratio of the A$_1$ modes of chalcopyrite-type CuInS$_2$ (292 cm^{-1}) and of CuAu-ordered CuInS$_2$ (305 cm^{-1}) as well as of the superpositioned B$_2{}^1_{LO}$/E$^1_{LO}$ modes of chalcopyrite CuInS$_2$ (340 cm^{-1}). For a) the area ratio A$_1$(chalcopyrite):A$_1$(CuAu-order):B$_2{}^1_{LO}$/E$^1_{LO}$(chalcopyrite) was determined as 26:53:21, whereas a ratio of 12:39:49 was obtained from the spectrum in b).

It was stated above (section 5.2.1.) that the intensity ratio of the A$_1$ mode of CuAu-ordered CuInS$_2$ maybe influenced by the possible presence of CuIn$_5$S$_8$, InS or β- and α-In$_2$S$_3$ if additional modes at 349 cm^{-1}, 215 cm^{-1} and 266 cm^{-1} were observed, respectively. No such modes were observed at 215 cm^{-1} and 266 cm^{-1}, so that the presence of InS or β- and α-In$_2$S$_3$ can be excluded. However, the strong contribution of the E$^1_{LO}$ and B$_2{}^1_{LO}$ modes could be caused by an additional contribution at 349 cm^{-1} of CuIn$_5$S$_8$ that may be present in the films. However, it will be argued in the next section that this case can also be excluded. Consequently, the Raman spectra can be concluded to be solely caused by the contributions of chalcopyrite-type and CuAu-ordered CuInS$_2$.

In Fig. 5.10, the peak area ratio of the A$_1$ modes of chalcopyrite-type and CuAu-ordered CuInS$_2$ as determined from the Raman spectra obtained from the homogeneous and inhomogeneous regions of as-deposited Spray ILGAR CuInS$_2$ thin films are shown.
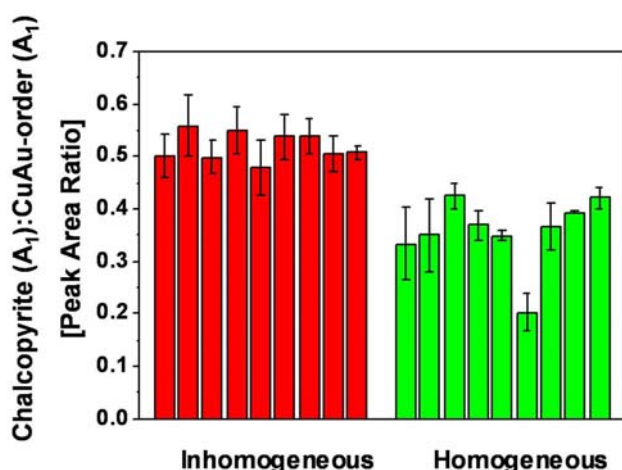

Fig. 5.10:   Bar diagram of the peak area ratio of the A$_1$ modes of chalcopyrite-type and CuAu-ordered CuInS$_2$ in the Raman spectra obtained on the homogeneous and inhomogeneous regions of as-deposited Spray ILGAR CuInS$_2$ thin films (sample 329, 330, 412-418; Appendix I). In order to avoid damping effects by Cu$_{2-x}$S, all films were etched in KCN. The error bars represent the scattering observed in five measurements in the respective region of the film.

The error bars reflect the scattering of the determined peak area ratios obtained from five measurements on the same region (homogeneous or inhomogeneous) of each sample. It can be seen from Fig. 5.10 that for the inhomogeneous regions of the as-deposited Spray ILGAR CuInS$_2$ thin films the peak area ratio of the A$_1$ modes of chalcopyrite-type and CuAu-ordered CuInS$_2$ varied between 0.43 and 0.62 (mean value of 0.52), whilst for the homogeneous

103

regions, ratios between 0.17 and 0.41 (mean value 0.36) were obtained. These values show that independently of the preparation parameters of a given thin film, the contribution of the A$_1$ mode of CuAu-ordered CuInS$_2$ is stronger for the homogeneous regions of the film compared to the inhomogeneous region. Consequently, the homogeneous regions can be assumed to contain a higher content of CuAu-ordered CuInS$_2$ than the inhomogeneous regions. Based on the model for the growth of Spray ILGAR CuInS$_2$ thin films deduced in chapter 4 (section 4.5.), this can be interpreted as follows.

In chapter 4, the homogeneous regions of the film were found to be In$_2$O$_3$-rich, whilst the inhomogeneous regions are CuInS$_2$-rich (both CuInS$_2$ phases) (Fig. 4.15). In particular, it was shown that the surface of the homogeneous regions solely consists of In$_2$O$_3$ (Fig. 4.16), whereas the inhomogeneous regions were covered by Cu$_{2-x}$S agglomerates. Therefore, it was concluded that the segregation of the Cu$_{2-x}$S agglomerates occurs via copper diffusion through the CuInS$_2$ domains, i.e. the inhomogeneous regions of the films. Now, the following conclusions can be drawn from the Raman spectroscopic studies in the present section:

o In the Raman spectra obtained from the homogeneous (In$_2$O$_3$-rich) regions, chalcopyrite-type and CuAu-ordered CuInS$_2$ were detected. Since the surface of these regions was shown to consist of In$_2$O$_3$, this means that CuInS$_2$ is only present in the lower parts of the homogeneous regions of the film. Thus, the In$_2$O$_3$ content (relative to CuInS$_2$) decreases in depth in the homogeneous regions.

o The increased content of chalcopyrite-type CuInS$_2$ in the inhomogeneous regions compared to the inhomogeneous regions of the films can be attributed to the segregation of Cu$_{2-x}$S and CuS that occurs via copper diffusion through the inhomogeneous regions of the film. Such a segregation of copper sulfide phases was found to lead to a recrystallization of CuInS$_2$ in the growth of RTP-CuInS$_2$ thin films, which led to a reduced amount of CuAu-ordered CuInS$_2$ in these films [Neisser_2 '01; Rudigier_1 '04]. Thus, it is suggested, that the copper sulfide segregation out of the inhomogeneous regions of the film leads to the observed increased amount of chalcopyrite-type CuInS$_2$ in these regions.

o The observation that the contribution of the A$_1$ mode of CuAu-ordered CuInS$_2$ to the Raman spectra exceeded the contribution of the A$_1$ mode of chalcopyrite-type CuInS$_2$ is likely due to the moderate deposition temperature of 430 °C used for the deposition of the films. Several authors showed that the formation of CuAu-ordered CuInS$_2$ is favored at the expense of chalcopyrite-type CuInS$_2$ at growth temperatures below 500 °C [Alvarez-Garcia_1 '01; Riedle '02; Rudigier_1 '04; Rudigier '05].

Increased Intensity of the E^1_{LO} and $B_2{}^1_{LO}$ modes of chalcopyrite-type CuInS$_2$

As shown in Fig. 5.8a and Fig. 5.9b, the relative intensities of the superimposed E^1_{LO} and $B_2{}^1_{LO}$ modes of chalcopyrite-type CuInS$_2$ were increased in the Raman spectra of as-deposited Spray ILGAR CuInS$_2$ thin films compared to single-phase RTP-prepared thin films of chalcopyrite-type CuInS$_2$ (Fig 5.2a). In Fig. 5.11, the ratio of the total peak area of both A$_1$-modes (chalcopyrite-type and CuAu-ordered CuInS$_2$) and the peak area of the superimposed E^1_{LO} and $B_2{}^1_{LO}$ modes of chalcopyrite-type CuInS$_2$ is shown as determined from the fits of the Raman spectra obtained from the homogeneous and inhomogeneous regions of nine as-deposited Spray ILGAR CuInS$_2$ thin films (samples 329, 330, 412-418; Appendix I). The contribution of the E^1_{LO} and $B_2{}^1_{LO}$ modes of chalcopyrite-type CuInS$_2$ is particularly high (low ratio in Fig. 5.11) for the Raman spectra that were obtained from the homogeneous regions of the films. For the homogeneous regions ratios between 0.9 and 1.4 (mean value: 1.1) were obtained, whilst for the inhomogeneous regions the ratio varied between 1.2 and 3.2 (mean value: 2.2).
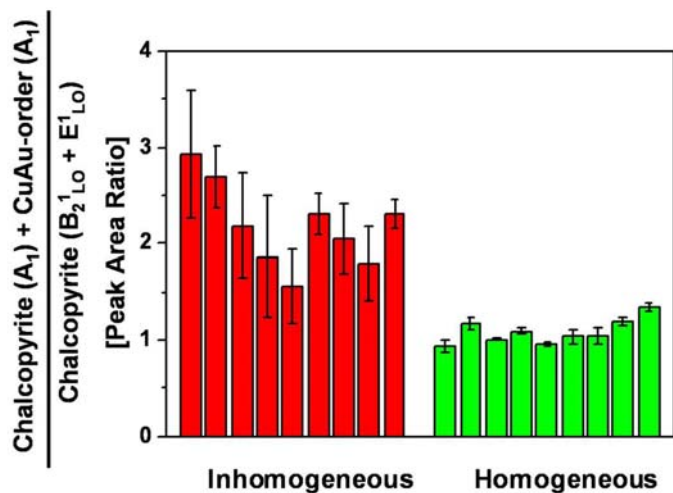
Fig. 5.11: Ratio of the total peak area of both A$_1$ modes (chalcopyrite-type and CuAu-ordered CuInS$_2$) and the peak area of the E$^1_{LO}$ and B$_2$$^1_{LO}$ modes of chalcopyrite-type CuInS$_2$ as determined from Raman spectra obtained on the inhomogeneous and homogeneous parts of as-deposited Spray ILGAR CuInS$_2$ thin films (sample 329, 330, 412-418; Appendix I). All films were KCN etched to avoid damping effects by Cu$_{2-x}$S. The error bars represent the scattering of five measurements in the respective region of each film.

In contrast, for single-phase chalcopyrite-type thin films, the contribution of the E$^1_{LO}$ and B$_2$$^1_{LO}$ modes to the Raman spectrum are very low (Fig. 5.2a). The peak area of the E$^1_{LO}$ and B$_2$$^1_{LO}$ modes was found to only amount to about 5 % of the area of the A$_1$ mode for reference RTP-CuInS$_2$ thin films in the course of this work. Therefore, the origin of the increased contribution of the E$^1_{LO}$ and B$_2$$^1_{LO}$ modes of chalcopyrite-CuInS$_2$ to the Raman spectrum of as-deposited Spray ILGAR CuInS$_2$ thin films is discussed.

Based on the above considerations (section 5.2.1.) about the influence of secondary phases on the CuInS$_2$ Raman spectrum and on published reports about Raman spectroscopy of chalcopyrite-type materials, several explanations for the increased contribution of the E$^1_{LO}$ and B$_2$$^1_{LO}$ modes may be given, which will be assessed in the following:

Firstly, the increased intensities of these modes could be attributed to secondary phases, which maybe present in the films. The considerations in section 5.2.1. revealed that only the presence of CuIn$_5$S$_8$, InS or β- and α-In$_2$S$_3$ has to be taken into account. Of these phases, InS or β- and α-In$_2$S$_3$ can be excluded, since the main peaks of these modes located at 215 cm^{-1} and 266 cm^{-1} were not observed in the Raman spectra. Also CuIn$_5$S$_8$ can be excluded, even though its most intense mode (F$_{23}$) is located close (349 cm^{-1}) to the wavenumber range of the E$^1_{LO}$ and B$_2$$^1_{LO}$ modes. It will be shown, however, in the next section (section 5.2.3.), that the intensity of the E$^1_{LO}$ and B$_2$$^1_{LO}$ modes decreases strongly upon a post-deposition H$_2$S annealing of the Spray ILGAR CuInS$_2$ thin films. Since CuIn$_5$S$_8$ is known to be stable up to 1085 °C (Fig. 2.4), this excludes the possibility of a contribution of this phase to the Raman spectra of the as-deposited Spray ILGAR CuInS$_2$ thin films.

A second explanation for the increased contribution of the E$^1_{LO}$ and B$_2$$^1_{LO}$ modes of chalcopyrite-type CuInS$_2$ to the Raman spectrum of as-deposited Spray ILGAR CuInS$_2$ thin films may be given by reports of Xue *et al.* [Xue '04]. These authors observed that in structurally similar PVD-grown CuGaSe$_2$ thin films, the relative intensities of the E$^1_{LO}$ and B$_2$$^1_{LO}$ modes increased compared to the intensity of the A$_1$-mode of chalcopyrite-type CuGaSe$_2$ for films, whose stoichiometry deviated from the ideal CuGaSe$_2$ stoichiometry of [Cu]:[Ga]:[Se] = 1:1:2. Xue *et al.* supposed that due to the different symmetries of the A$_1$, E$^1_{LO}$ and B$_2$$^1_{LO}$ modes (Appendix XI; Fig. XI.1), they couple to different electronic bands. Therefore, changes in the crystalline order induced by stoichiometric deviations or impurities may cause the observed increase of the relative intensities of the E$^1_{LO}$ and B$_2$$^1_{LO}$ modes.

This explanation is also applicable to the Spray ILGAR CuInS$_2$ thin films investigated in this section and is further supported by the observation that the increased intensity of the E$^1_{LO}$ and B$_2$$^1_{LO}$ modes is particularly pronounced in the homogeneous regions of the Spray ILGAR CuInS$_2$ thin films. These regions exhibit an increased In$_2$O$_3$- and a decreased CuInS$_2$ content. Therefore, the degree of disorder can also be expected to be increased in the homogeneous regions. The dependence of the relative intensities of the E$^1_{LO}$ and B$_2$$^1_{LO}$ modes of

chalcopyrite-type CuInS$_2$ in as-deposited Spray ILGAR CuInS$_2$ thin films can also be seen in Fig. 5.12. Here, the ratio of the total peak area of both A$_1$-modes (chalcopyrite-type and CuAu-ordered CuInS$_2$) and the peak area of the superimposed E$^1_{LO}$ and B$_2$$^1_{LO}$ modes of chalcopyrite-type CuInS$_2$ is shown on the *y-axis*. This ratio reflects the *inverse relative contributions of the E$^1_{LO}$ and B$_2$$^1_{LO}$ modes* to the Raman spectrum. On the *x-axis*, the peak area ratio of the A$_1$-modes of chalcopyrite-type and CuAu-ordered CuInS$_2$ is given. This ratio reflects the chalcopyrite content of the probed region of the film and thus its *phase purity*.

Fig. 5.12:   Influence of the chalcopyrite phase purity on the contribution of the E$^1_{LO}$ and B$_2$$^1_{LO}$ modes of chalcopyrite-type CuInS$_2$. The peak area ratio of the combined A$_1$-mode (chalcopyrite and CuAu-order) to the E$^1_{LO}$ and B$_2$$^1_{LO}$ modes of chalcopyrite-type CuInS$_2$ (*reflecting the inverse contribution of these modes to the Raman spectrum*) is shown as a function of the peak area ratio of the A$_1$-modes of chalcopyrite-type and CuAu-ordered CuInS$_2$ (*reflecting the chalcopyrite phase purity of the probed sample volume*). The Raman spectra were recorded on the homogeneous (black open symbols) and inhomogeneous (red full symbols) regions of as-deposited KCN etched Spray ILGAR CuInS$_2$ thin films (samples 329, 330, 412-418; Appendix I). The error bars result from the standard deviations of five measurements performed on the same region of each film.

Fig. 5.12 shows that the contribution of the E$^1_{LO}$ and B$_2$$^1_{LO}$ modes of chalcopyrite-type CuInS$_2$ in as-deposited Spray ILGAR CuInS$_2$ thin films decreases as the chalcopyrite phase purity increases in the probed sample area. This supports the theory of Xue *et al.* [Xue '04] that the intensity of the E$^1_{LO}$ and B$_2$$^1_{LO}$ modes of chalcopyrite-type compounds increases as the degree of disorder in the sample increases. This interpretation also agrees with observations of Enzenhofer, who observed an increase of the E$^1_{LO}$ and B$_2$$^1_{LO}$ modes of chalcopyrite-type CuInS$_2$ in RTP-processed CuInS$_2$ thin films upon doping the films with zinc and thus increasing the disorder in the films [Enzenhofer '07].

5.2.3.   Raman Spectroscopy of H$_2$S treated Spray ILGAR CuInS$_2$ Thin Films

In this section, the influence of the post-deposition H$_2$S annealing on the Raman spectrum of Spray ILGAR CuInS$_2$ thin films is investigated. It was shown that after this annealing, the films consist of two differently crystallized regions: a *well-crystallized top layer* and a *layered bottom layer* (Fig. 3.13b, d). It was further shown that the H$_2$S annealed films did not contain In$_2$O$_3$, but only consisted of CuInS$_2$ (chalcopyrite-type and CuAu-ordered) (Fig. 3.11) and the carbon-containing interlayers in the *layered bottom layer* (Fig. 4.17). Furthermore, Cu$_{2-x}$S ($0 \leq x \leq 0.2$) was also found in the films, which is removed by a subsequent KCN etching.

In this section, the structural properties of the *well-crystallized top layer* and the *layered bottom layer* are separately investigated by Micro-Raman spectroscopy. Both lateral and

depth variations of the distribution of CuAu-ordered CuInS$_2$ in these films are undertaken to study the homogeneity of the Spray ILGAR CuInS$_2$ thin films.

Lateral Variations of the Distribution of CuAu-ordered CuInS$_2$

Due to the limited information depth of about 150 nm (for λ = 632.8 nm; section 5.1.4.) in Raman spectroscopic investigations of CuInS$_2$, such measurements only probe the upmost 150 nm of the films. Since during the post-deposition H$_2$S annealing, the *well-crystallized top layer* is formed on top of the *layered bottom layer* (Fig. 4.18), Raman spectroscopy provides a convenient way to study the structural properties of this layer and to compare them to the properties of the as-deposited films.

In Fig. 5.13, Raman spectra and optical micrographs of a Spray ILGAR CuInS$_2$ thin film (Sample 418) are shown, which was deposited using such parameters (Appendix I) that the *well-crystallized top layer* was not completely closed but consisted of grains of diameters of several hundred nanometers that partially covered the *layered bottom layer*. The Raman spectra and optical micrograph in Fig. 5.13a and b were recorded on the as-deposited film, whilst Fig. 5.13c and d and Fig. 5.13e and f were obtained from the H$_2$S treated and H$_2$S and KCN treated film, respectively.
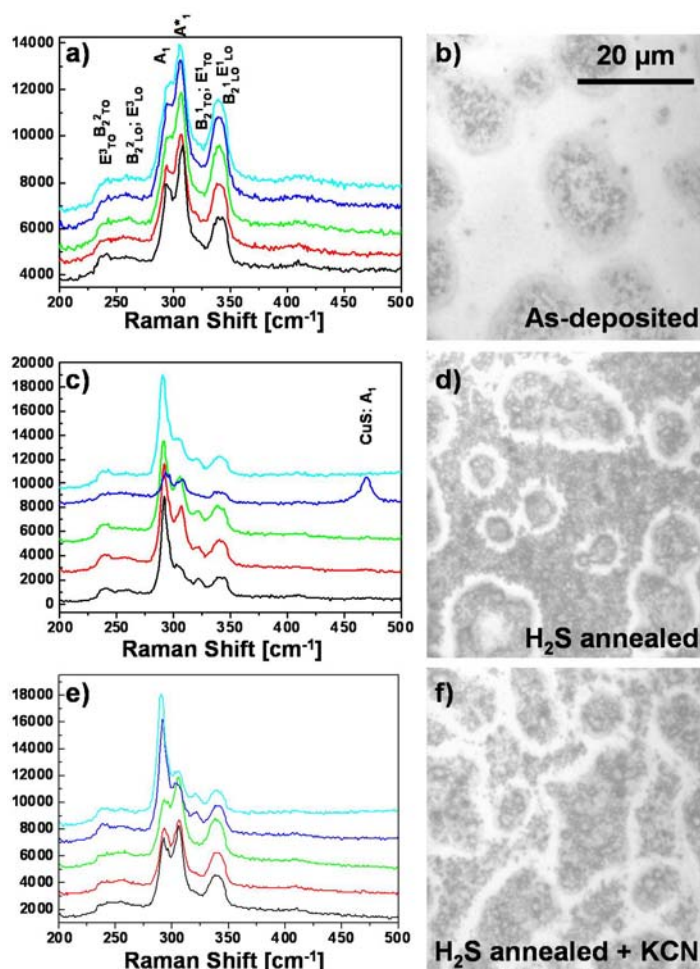

Fig. 5.13: Raman spectra and optical micrographs of an as-deposited Spray ILGAR CuInS$_2$ thin film (sample 418) in its as-deposited state (a, b), after the post-deposition H$_2$S annealing (c, d) and after H$_2$S annealing and KCN etching (e, f). Note that the images are not recorded at the same location of the film after different treatments, but on different parts of the same film that were treated differently. The Raman spectra were recorded at five different spots (diameter 1-2μm) spots. In a), the black and red spectra were recorded on the inhomogeneous regions of the film, whilst the green, cyan and blue spectra were recorded on the homogeneous regions. For b) and c), both regions contributed to the spectra, due to the deceased area of the homogeneous region after H$_2$S annealing. The spectra are shifted on the intensity axis for the sake of clarity. The Raman modes of chalcopyrite-type and CuAu-ordered (*) CuInS$_2$ and CuS are indicated in a), c) and e) The preparation parameters are listed in Appendix I.

The Raman spectra of the as-deposited Spray ILGAR CuInS$_2$ thin film (Fig. 5.13a) were recorded on the homogeneous (green, cyan and blue trace) and on the inhomogeneous regions (red and black trace) of the film. These spectra are in accordance with those discussed in section 5.2.2., as the contribution of the A$_1$ mode of CuAu-ordered CuInS$_2$ exceeds that of the A$_1$ mode of chalcopyrite-type CuInS$_2$. Furthermore, increased contributions of the E$^1_{LO}$ and

$B_2{}^1{}_{LO}$ modes of chalcopyrite-type CuInS$_2$ was observed for the spectra obtained from the homogeneous regions of the film as it was discussed above. Upon H$_2$S annealing, changes of the Raman spectra as well of the surface morphology can be observed. The grains of the *well-crystallized top layer* cover most of the surface, so that the homogeneous region of the film is reduced to narrow regions (about 1 μm) around the grains of the *well-crystallized top layer* (bright areas in Fig. 5.13e). Due to the narrowness of these regions, the homogeneous areas of the film could not be separately probed by Raman spectroscopy, anymore. Therefore, the spectra in Fig. 5.13c and e were recorded at five arbitrarily chosen spots on the film surface. After a subsequent KCN etching, no significant changes in the morphology are observed. It can be seen that in the Raman spectra of the H$_2$S treated (Fig. 5.13c) and of the H$_2$S and KCN treated (Fig. 5.13c) film, the intensity of the A$_1$ mode of chalcopyrite-type CuInS$_2$ exceeds that of the A$_1$ mode of CuAu-ordered CuInS$_2$, which is in contrast to the behavior observed in the as-deposited film (Fig. 5.13a). Thus, the formation of the *well-crystallized top layer* during the post-deposition H$_2$S annealing increases the amount of chalcopyrite-type CuInS$_2$ in the Spray ILGAR CuInS$_2$ thin films. This may occur by different mechanisms:

o The H$_2$S annealing may partially convert the metastable CuAu-ordered CuInS$_2$ into chalcopyrite-type CuInS$_2$. Such a behavior has been observed in H$_2$S annealed CuInS$_2$ thin films deposited by spray pyrolysis [Krunks '06].

o Alternatively, it may be assumed that the additional CuInS$_2$ in the *well-crystallized top layer*, which is formed during the post-deposition annealing (Fig. 4.20), consists of chalcopyrite-type CuInS$_2$. After the H$_2$S annealing this newly formed chalcopyrite-type CuInS$_2$ covers the *layered bottom layer*, which still contains the same amount of CuAu-ordered CuInS$_2$.

o Since both mechanisms do not exclude each other, also a combination of both is possible.

Which of these mechanisms accounts for the increased chalcopyrite content in the H$_2$S treated Spray ILGAR CuInS$_2$ thin films is discussed in the following. In section 4.4.2.5., the influence of the preparation and annealing conditions on the properties of the *well-crystallized top layer* of Spray ILGAR CuInS$_2$ was studied. Thereby, Spray ILGAR CuInS$_2$ thin films were prepared (samples 419-421; Fig. 4.18; Appendix I), whose *well-crystallized top layers* showed different thicknesses and different degrees of lateral homogeneity. Therefore, these films are well-suited for the investigation of the distribution of chalcopyrite-type and CuAu-ordered CuInS$_2$ in the *well-crystallized top layer*. In Fig. 5.14, Raman spectra (a, d, g), plan-view optical micrographs (b, e, h) and cross-sectional SEM images (c, f, i) obtained from these samples are shown. The Raman spectra in Fig 5.14a, d and g were recorded at five arbitrarily chosen spots on each film.

The *well-crystallized top layer* of sample 419 was not completely closed (Fig 5.14b) and consisted of grains with diameters of 100-400 nm (Fig 5.14c). In the Raman spectra obtained from this film (Fig. 5.14a), comparable contributions of the A$_1$ modes of CuAu-ordered (A*$_1$ in Fig 5.14) and chalcopyrite-type CuInS$_2$ are observed in several spectra.

In contrast, the *well-crystallized top layer* of sample 420 completely covered the *layered bottom layer* (Fig. 5.14e). The grain size in this *top layer* varied between 100 nm and 600 nm (Fig. 5.14e). In the Raman spectra recorded on this film, the contribution of the A$_1$ mode of chalcopyrite-type CuInS$_2$ exceeded that of the A$_1$ mode of CuAu-ordered CuInS$_2$ in all spectra, but non-zero contributions of CuAu-ordered CuInS$_2$ were still observed in the spectra (Fig. 5.14d).

For sample 421, the *well-crystallized top layer* also covered the *layered bottom layer* completely (Fig. 5.14h), but it thickness was further increased and varied between 500 nm and 1000 nm (Fig. 5.14i). For this film, only negligible contributions of the A$_1$ mode of CuAu-ordered CuInS$_2$ thin films were observed. The obtained spectra matched well with those obtained from single-phase RTP-processed chalcopyrite-type CuInS$_2$ thin films (Fig. 5.2a).
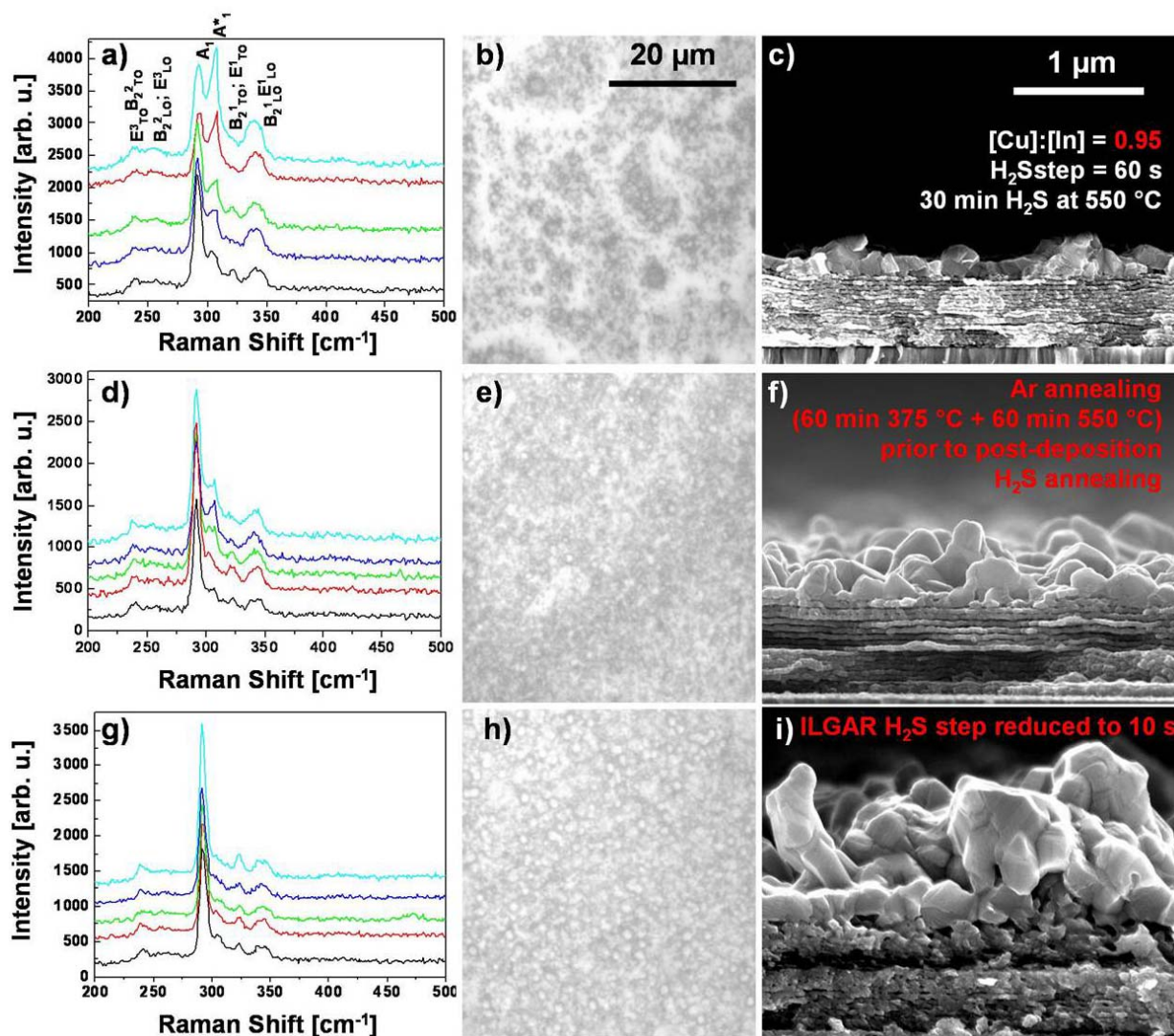
Fig. 5.14:   Raman spectra (a, d, g), optical plan-view (b, e, h) and SEM cross-sectional (c, f, i) micrographs of H$_2$S annealed Spray ILGAR CuInS$_2$ thin films with *well-crystallized top layers* of different thickness (samples 419-421; compare Fig. 4.18). The Raman spectra were measured at five different arbitrarily chosen spots (diameter 1-2μm). See Appendix I for preparation parameters. The Raman modes of chalcopyrite-type and CuAu-ordered (*) are marked in the spectra. The spectra are shifted on the intensity scale for the sake of clarity. All optical and SEM micrographs are shown on the same scale, respectively.

Thus, in conclusion, the analysis of the Raman spectra of theses samples (samples 419-421; Fig. 5.14) shows that the contribution of the A$_1$ mode of CuAu-ordered CuInS$_2$ decreases as the homogeneity and thickness of the *well-crystallized top layer* increases. This indicates that the *well-crystallized top layer* consists of chalcopyrite-type CuInS$_2$ and only contains negligible amounts of CuAu-ordered CuInS$_2$. In order to verify this assumption and to directly compare the distribution of CuAu-ordered CuInS$_2$ in the *well-crystallized top layer* and in the *layered bottom layer*, the variations of the distribution of CuAu-ordered CuInS$_2$ in depth in the Spray ILGAR CuInS$_2$ thin films are studied in the following section.

Variations of the Distribution of CuAu-ordered CuInS$_2$ in Depth

In order to investigate how the distribution of CuAu-ordered and chalcopyrite-type CuInS$_2$ evolves in the depth of the Spray ILGAR CuInS$_2$ thin films, the film exhibiting the thickest *well-crystallized top layer* of 500-1000 nm (sample 421, Fig. 5.14g-i) was peeled of from the

molybdenum-covered substrate by applying the *Lift-off-process* [Fuertes Marron '05]. Thus, also the backside of this film could be investigated by Raman spectroscopy. Since the thickness of the *well-crystallized top layer* exceeded the information depth of the exciting laser (about 150 nm), it was ensured that the Raman measurements at the frontside solely probed the *well-crystallized top layer*, whilst those at the backside exclusively probed the *layered bottom layer*. This allowed the direct comparison of the contributions of chalcopyrite-type and CuAu-ordered CuInS$_2$ to the Raman spectra of both regions of the film. In Fig. 5.15, Raman spectra as obtained from the front- and backside are shown, which reflect the properties of the *well-crystallized top layer* and of the *layered bottom layer*, respectively.
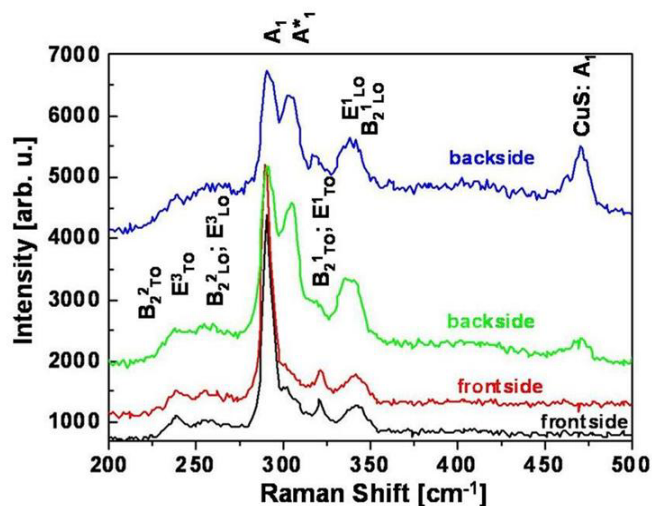

Fig. 5.15: Raman spectra obtained at two different spots on the front- and backside of an H$_2$S and KCN treated Spray ILGAR CuInS$_2$ thin film (sample 421). The backside spectra solely probe the *layered bottom layer* of the films, whilst the frontside spectra exclusively probe the *well-crystallized top layer* of the films. The asterisk* marks the A$_1$-mode of CuAu-ordered CuInS$_2$. Also the A$_1$ mode of CuS is indicated. All other modes belong to the chalcopyrite modification of CuInS$_2$. The spectra are shifted on the intensity axis for the sake of clarity. The preparation parameters are listed in Appendix I.

For each side of the film two typical spectra recorded at different locations are shown. The spectra obtained from the backside, which probe the *layered bottom layer* of the film, show a significant contribution of CuAu-ordered CuInS$_2$. The peak area ratio of the A$_1$ modes of chalcopyrite-type and CuAu-ordered CuInS$_2$ was found to vary between 0.70 and 1.16 (mean value of 0.89) for these spectra. In contrast, the Raman spectra obtained from the film frontside, which probe the *well-crystallized top layer*, only show negligible contributions of CuAu-ordered CuInS$_2$. This result supports the above assumption that the *well-crystallized top layer* consists of chalcopyrite-type CuInS$_2$. However, also the peak area ratio of the A$_1$ modes of chalcopyrite-type and CuAu-ordered CuInS$_2$ determined from the backside spectra (mean value 0.89) exceeds the ratios that were determined from the Raman spectra of the as-deposited Spray ILGAR CuInS$_2$ thin films (mean values 0.52 for the inhomogeneous region and 0.36 for the homogeneous region of the films; Fig. 5.10). Thus, the post-deposition H$_2$S annealing increases the amount of chalcopyrite-type CuInS$_2$, at the expense of CuAu-ordered CuInS$_2$, in the *layered bottom layer* of the Spray ILGAR CuInS$_2$ thin films.

In Fig. 5.15, an increased intensity of the E^1$_{LO}$ and B$_2^{1}_{LO}$ modes of chalcopyrite-type CuInS$_2$ can also be observed at the backside of the films, compared to the frontside spectra. According to the above results (Fig. 5.12), this corresponds to increased disorder and decreased phase purity of chalcopyrite-type CuInS$_2$ in these regions of the films, which agrees well with the small grain size (Fig. 5.14i) and the presence of the carbon-containing interlayers (Fig. 4.17) that are observed in the *layered bottom layer*.

Additionally, also small contributions of CuS are found on the backside of the films. Since CuS and Cu$_{2-x}$S ($0 \leq x \leq 0.2$) were found to segregate on the surface of the Spray ILGAR CuInS$_2$ thin films (see Fig. 4.14), this indicates that the CuInS$_2$ crystallization process was hindered in the *layered bottom layer* of the film. Since the segregation of CuS and Cu$_{2-x}$S ($0 \leq x \leq 0.2$) was concluded to occur via copper diffusion through the CuInS$_2$ domains of the *layered bottom layer*, the observation of CuS in the *layered bottom layer* may be due to the presence of carbon-containing interlayers (Fig. 4.17), which hinder the diffusion of copper. In the

following section (section 5.3.) it will be shown that the carbon interlayers consist of amorphous carbon and nanocrystalline graphite. These materials were found to allow no diffusion of copper below temperatures of 1000 °C [Jackson '95; Kröger '03] (Appendix V). The results about the depth-distribution of CuAu-ordered and chalcopyrite-type CuInS$_2$ in the H$_2$S treated Spray ILGAR CuInS$_2$ thin films presented in this section was further confirmed by Micro-Raman mappings[22] of the cross-sections of a H$_2$S treated Spray ILGAR CuInS$_2$ thin film, which are shown in Fig. 5.16.
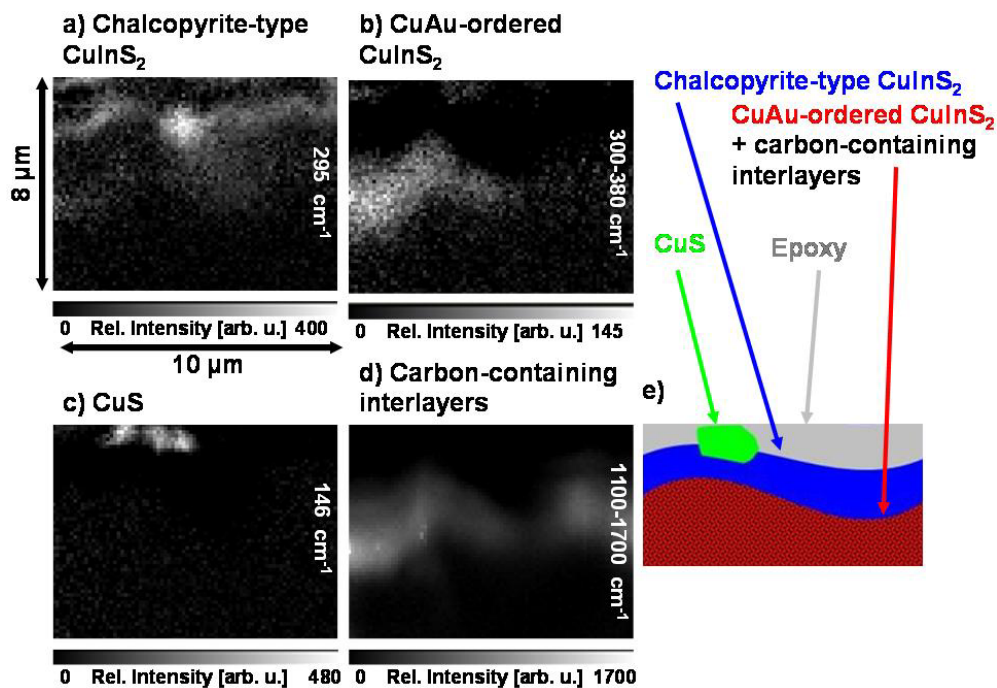
Fig. 5.16: Raman intensity maps obtained from a cross-section of a H$_2$S annealed Spray ILGAR CuInS$_2$ thin film (sample 420; Appendix I). The different maps depict the distribution of the different phases in the specimen: a) Chalcopyrite-type CuInS$_2$; b) CuAu-ordered CuInS$_2$; c) CuS; d) carbon-containing interlayers (see section 5.3.). The grayscales represents the relative intensity of the respective Raman signal (black: low intensity; white: high intensity). The spot diameter of the exciting laser of 500 nm determines the spatial resolution. In e) a schematic sketch of the cross-section is shown.

The Raman maps consist of 80x62 pixels, which each correspond to a Raman spectrum of a certain selected spectral range. The spatial resolution of the maps was determined by the spot diameter of 500 nm of the exciting laser. The integrated intensity of each spectrum is represented by the color of the respective pixel on a grayscale such that white corresponds to a high Raman intensity black to an intensity of zero. Thus, the distribution of various phases in the probed sample area can be depicted on a grayscale map. The Raman mappings in Fig. 5.16 were all obtained from the same area of the cross-section of a H$_2$S treated Spray ILGAR CuInS$_2$ thin film (sample 420; Fig. 5.14f; Appendix I). In Fig. 5.16a, the intensity distribution of the A$_1$ mode of chalcopyrite-type CuInS$_2$ is shown. In Fig. 5.16b, the intensity distribution of the spectral range of 300-380 cm^{-1} is shown. As shown above, this spectral range corresponds to the A$_1$ mode of CuAu-ordered CuInS$_2$ and the E$^1_{LO}$ and B$_2{}^1_{LO}$ modes of chalcopyrite-type CuInS$_2$. Since the intensities of the latter were found to increase with an increasing intensity of the A$_1$ mode of CuAu-ordered CuInS$_2$ (Fig. 5.12), this spectral range represents the contribution of CuAu-ordered CuInS$_2$ to the Raman spectrum. In Fig. 5.16c, the intensity distribution of the CuS is shown. This phase is represented by its Raman mode located at 146 cm^{-1} (symmetry not assigned; [Riedle '02; Munce '07]). Additionally, the

---

[22] The Raman mappings in Fig. 5.16 have been recorded by Dr. Thomas Schmid in the group of Prof. Dr. Renato Zenobi at the ETH Zürich.

intensity distribution of the spectral range of 1100-1700 cm^{-1} is shown in Fig. 5.16d. It will be shown in section 5.3. that this spectral range (D- and G-mode of carbon [Ferrari '00]) represents the carbon-containing interlayers.

In Fig. 5.16d, a schematic sketch of the phase distribution in the probed part of the cross-section of the H$_2$S treated Spray ILGAR CuInS$_2$ thin film is shown, which summarizes the results deduced from the Raman mappings. The observed phase distribution agrees with the results in Fig. 5.15 and confirms that chalcopyrite-type CuInS$_2$ is mainly found in the upper part of the H$_2$S treated Spray ILGAR CuInS$_2$ film, i.e. in the *well-crystallized top layer* (Fig. 5.16a). In contrast, CuAu-ordered CuInS$_2$ is mainly found in the lower layered part of the film (Fig. 5.16b), i.e. in the *layered bottom layer*. Additionally, CuS agglomerates are observed locally at the film surface (Fig. 5.16c). The presence of the carbon-interlayers in the *layered bottom layer* is also confirmed by the Raman-mappings (Fig. 5.16d).

5.3.   Carbon in Spray ILGAR CuInS$_2$ Thin Films

In this section, the carbon-containing interlayers, which were observed to separate the CuInS$_2$ layers in the *layered bottom layer* of the Spray ILGAR CuInS$_2$ thin films (Fig. 4.17), are investigated by Raman spectroscopy, in order to identify the phases in these interlayers. The carbon in these layers is assumed to originate from the decomposed hfac groups of the Cu(hfac)$_2$ compound used for the spraying solutions (Fig. 3.1).

The Raman modes of carbon-related compounds are usually observed at Raman shifts in the range of 1000-2000 cm^{-1} [Wang '90; Escribano '01; Sze '01]. Therefore, the spectral range of the Raman measurements was extended to 200-1700 cm^{-1} in order to characterize the carbon-rich interlayers.

Applying the *Lift-off-process* [Fuertes Marron '05] allowed the characterization of the carbon-containing interlayers, which were observed by energy-filtered TEM in the *layered bottom layer* of Spray ILGAR CuInS$_2$ thin films (Fig. 4.17). Typical Raman spectra obtained from the front- and backside of such a film (sample 421; Appendix I) are shown in Fig. 5.17.
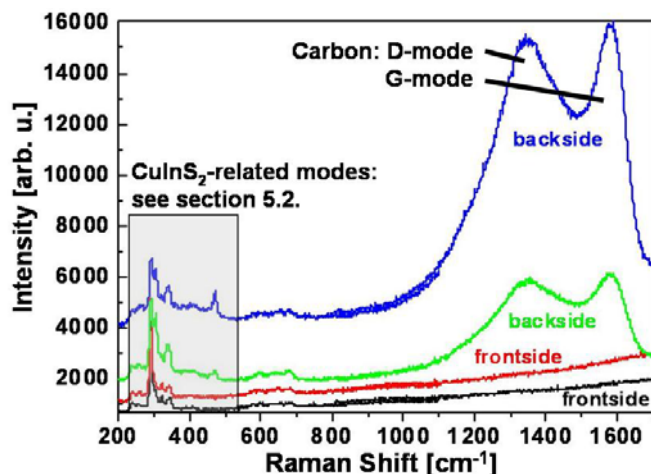

Fig. 5.17:   Raman spectra obtained at two different spots on the front- and backside of an H$_2$S and KCN treated Spray ILGAR CuInS$_2$ thin film (sample 421). The backside spectra solely probe the *layered bottom layer*, whilst the frontside spectra only probe the *well-crystallized top layer* of the film. The D- and G-modes of carbon are indicated. The gray box marks the spectral range of the CuInS$_2$-related Raman modes discussed in section 5.2. The spectra are shifted on the intensity axis for the sake of clarity. The preparation parameters are listed in Appendix I.

In the Raman spectra obtained from the backside of the Spray ILGAR CuInS$_2$ thin film, two broad peaks centered at around 1355 cm^{-1} and 1582 cm^{-1} were observed, which can be assigned to the D- and G-modes of carbon [Ferrari '00]. In contrast, these peaks were not observed in the frontside spectra. Thus, it is concluded that this carbon is located in the *layered bottom layer* of the film. Consequently, the carbon-containing interlayers observed by energy-filtered TEM in section 4.4.2.4. (Fig. 4.17) contain elemental carbon. TEM also revealed that these layers mostly consist of a phase of amorphous appearance (domain size blow 5 nm), in which larger particles with diameters in the range of 5-20 nm are dispersed (Fig. 5.18).
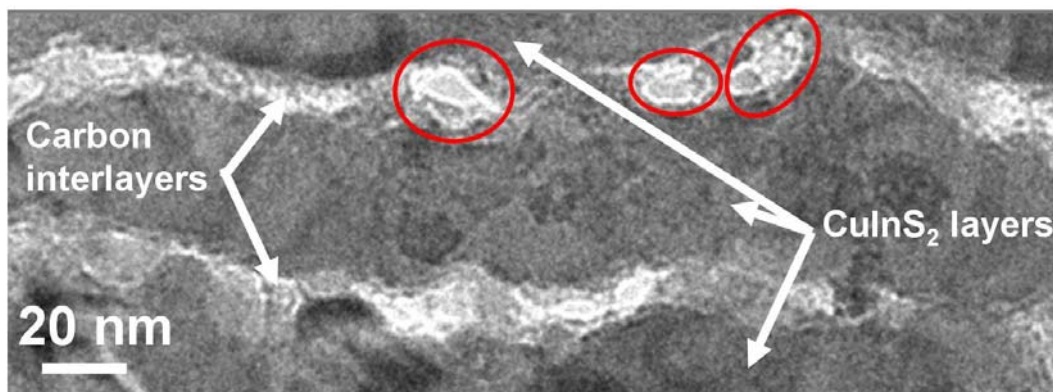
Fig. 5.18: Cross-sectional TEM image obtained from a H$_2$S annealed Spray ILGAR CuInS$_2$ thin film (sample 420). The preparation parameters are listed in Appendix I.

As shown by Ferrari and Robertson [Ferrari '00], the Raman spectrum of elemental carbon differs for the different existing modifications of carbon. In particular, the peak position of the G-mode and the intensity ratio of the D- and G-mode I_D/I_G can be used to identify a given carbon modification [Ferrari '00]. In the following, a brief overview about the classification and Raman spectroscopy of carbon materials is given as a basis for the analysis of the carbon Raman spectrum of the Spray ILGAR CuInS$_2$ thin films. This overview follows the argumentation in Ref. [Ferrari '00; Ferrari '01; Robertson '02; Ferrari '04; Casiraghi '05].

The physical properties of carbon materials are determined by the ratio of sp^2- (graphite-like) and sp^3-hybridized (diamond-like) carbon bonds. Generally, any mixture of sp^3, sp^2 and even sp^1 bonds may be present in carbon materials. The sp^1 phase was, however, observed to be stable only under UHV-conditions. Therefore, this phase is not considered any further in this discussion[23]. Besides the sp^2/sp^3 ratio, the properties of carbon materials are influenced by the possible presence of hydrogen (up to 60 at. %), i.e. of C-H bonds in the material. The key parameters for classifying such materials are the following:

- o   sp^3 content
- o   Clustering of the sp^2 phase
- o   Orientation of the sp^2 phase
- o   Nanostructure of the material
- o   H content

Depending on these parameters one can distinguish graphitic carbon and nanocrystalline graphite (NC-G) as well as sp^2-dominated amorphous carbon (a-C), tetrahedral amorphous carbon (ta-C) and diamond-like carbon (DLC). Furthermore, hydrogenated phases of a-C (a-C:H) and ta-C (ta-C:H) exist. The compositions of these phases can be shown as a quasiternary phase diagram (Fig. 5.19a; taken from Ref. [Ferrari '04]).

The Raman spectrum of all carbon materials can be described according to the *three-stage model of increasing disorder* introduced by Ferrari and Robertson [Ferrari '00] (Fig. 5.19b; taken from Ref. [Ferrari '04]). This model distinguishes three stages of *amorphization* moving from perfectly ordered graphite to NC-C (stage 1), to a-C (stage 2) and finally to ta-C (stage 3). Thereby, firstly, the sp^2 groups in the material become smaller (stage 1), then topologically disordered (stage 2) and finally their bonds change from ring to chain configuration (stage 3). Along these stages, the Raman spectrum is influenced by the following parameters:

- o   Clustering of the sp^2 phase
- o   Bond length and bond angle disorder
- o   Presence of sp^2 rings or chains
- o   sp^2/sp^3 ratio

---

[23] Since in this section, the carbon content of non-vacuum-processed CuInS$_2$ thin films is discussed, the presence of the UHV-stable sp^1 phase was not considered any further.

How these effects influence the Raman spectrum of carbon materials for an excitation wavelength of $\lambda = 633$ nm is indicated in Fig. 5.19c (taken from Ref. [Ferrari '00]) and explained subsequently.
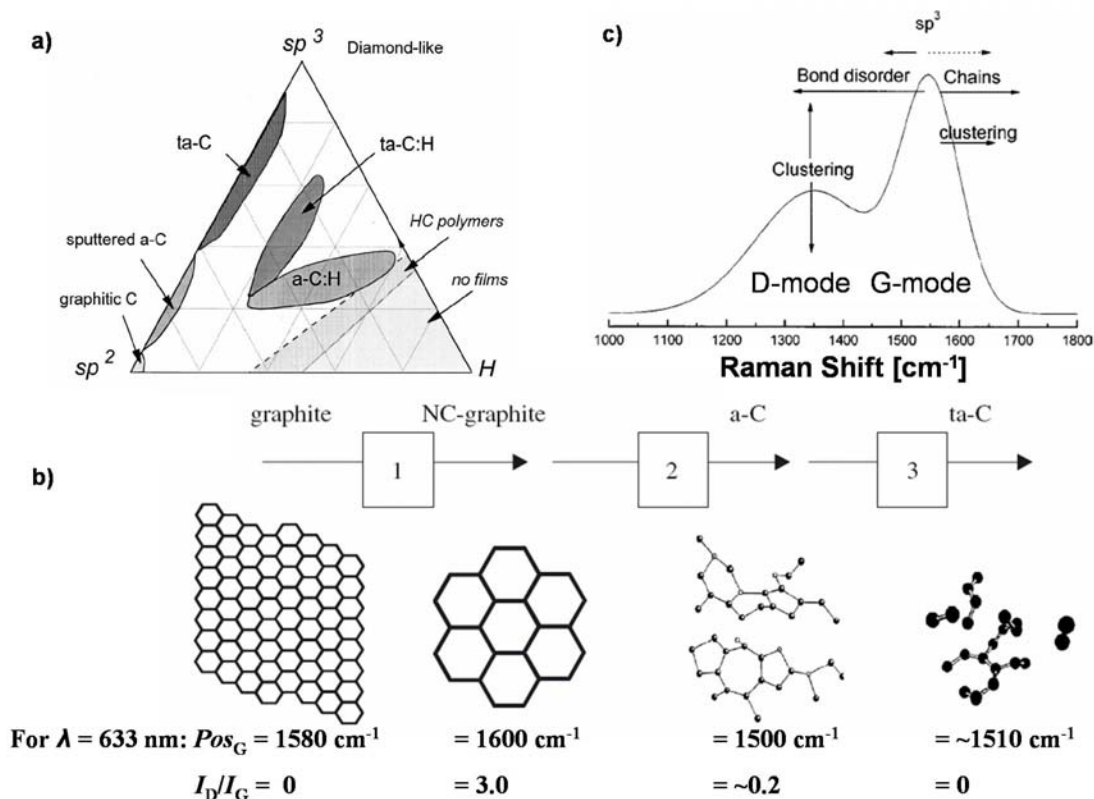

Fig. 5.19:   a) Quasiternary phase diagram for carbon materials. b) Three-stage-model for the amorphization of carbon from graphite to ta-C. c) Influence of the different stages of the three-stage model on the carbon Raman spectrum, in particular on the G-mode position and on the peak intensity ratio I_D/I_G of the D- and G-mode. The images a)-c) are taken from Ref. [Ferrari '00], [Ferrari '00] and [Ferrari '04], respectively.

The G-mode of carbon has E_2 symmetry. It is caused by the relative vibration of two sp^2 carbon atoms and therefore does not require the presence of complete sixfold rings as they exist in the lattice planes of graphite. Therefore, the G-mode is observed in all carbon materials containing sp^2 carbon. The precise position of this mode is, however, sensitive to the bond disorder of the sp^2 carbon atoms. As the domain size decreases in stage 1, the G-mode shifts from 1580 cm⁻¹ to 1600 cm⁻¹ (*clustering* in Fig. 5.19c). In stage 2, the weakening of the sp^2 bonds shifts the G-mode to a position of about 1500 cm⁻¹ (*bond disorder* in Fig. 5.19c). In stage 3, the coordination of the sp_2 bonds changes from rings to chains. Thereby, the G-mode moves slightly upwards to 1510 cm⁻¹, due to electron confinement in short chains (*chains* in Fig. 5.19c).

The D-mode is a breathing mode of A_1 symmetry of graphitic rings, but is forbidden in the perfect graphite lattice. It only shows a non-zero intensity, if disorder is present in sp^2 containing carbon material. Therefore, I_D/I_G evolves from 0 to 3.0 during stage 1, but decreases to about 0.2 in stage 2, when topological disorder is introduced. In stage 3 the rings are broken and thus I_D/I_G vanishes as their number decreases.

If hydrogen is present in a-C:H, it increases the sp^3 content in the material by saturating C=C as CH_x groups rather than increasing the fraction of C-C sp^3 bonds. For ta:H, the hydrogen leads to a stronger increase of the C-C sp^3 bonds compared to aC:H at a constant sp^3 level. In NC-G, introduced hydrogen breaks the graphite bonds and thus increases the bond angle and bond length disorder. However, if the hydrogen content exceeds 20 %, the breaking of the sp^2

bonds becomes so pronounced that it actually lowers the structural disorder, while the bond angle disorder increases.

Additionally, annealing effects may also affect the Raman spectrum since annealing leads to ordering in the carbon material. Thereby, a hysteris effect of the G-mode position and I_D/I_G was observed such that, if a ta-C film is converted to NC-G by annealing, the G-mode directly shifts from 1510 cm^{-1} to 1600 cm^{-1} and I_D/I_G evolves directly from 0 to 3.0 without passing the a-C values of 1500 cm^{-1} and 0.2 at the same time.

From these considerations, it follows that the exact sp^3/sp^2 ratio cannot be determined unambiguously from a single Raman spectrum. For a precise determination of this ratio, the dispersion of the G-mode, which is observed in Raman spectra recorded at different wavelengths including UV excitation are needed [Ferrari '00; Ferrari '01; Robertson '02; Ferrari '04; Casiraghi '05].

However, depending on the range of the observed G-mode positions and with additional information from the TEM measurements (Fig. 5.18), some conclusions may also be drawn from Raman spectra recorded at a single wavelength in the visible range.

In the following, the G-mode positions and I_D/I_G ratios determined from Raman spectra, which were obtained from Spray ILGAR CuInS$_2$ thin films using an excitation wavelength of λ = 632.8 nm, are interpreted with respect to the carbon phase present in the films. In Fig. 5.20, a typical Raman spectrum obtained from the backside of a H$_2$S and KCN treated Spray ILGAR CuInS$_2$ thin film is shown. The D- and G-modes were fitted by Lorentzians.
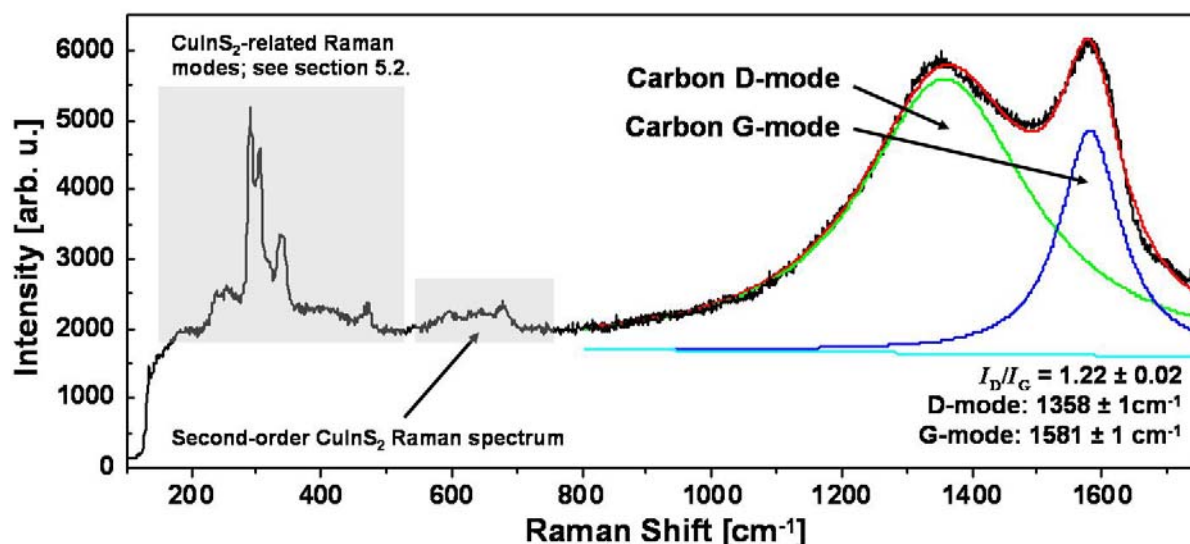

Fig. 5.20: Raman spectrum (black curve) obtained from the backside of an H$_2$S and KCN treated Spray ILGAR CuInS$_2$ thin film (sample 421; Appendix I). The contributions of the D- and G-modes were determined by fitting the spectrum by Lorentzians (green and blue curves; cyan: linear background). From this fit, the positions of the D- and G-mode were determined as 1358±1 cm^{-1} and 1581±1 cm^{-1}, respectively. The I_D/I_G ratio was 1.22 ± 0.02. The gray boxes mark the CuInS$_2$-related part of the spectrum, which are not considered in this section.

It was observed that compared to the parameter range, in which the G-positions (1500-1600 cm^{-1}) and I_D/I_G ratios (0-3) can vary for the various carbon modifications (Fig. 5.19c), only small variations were observed in the Raman Spectra obtained from Spray ILGAR CuInS$_2$ thin films, independently of the precise preparation parameters. Thereby, as-deposited (samples 329, 420), as well as H$_2$S annealed (samples 419, 421) Spray ILGAR CuInS$_2$ thin films were investigated. G-mode positions between 1574 ± 1 cm^{-1} and 1581 ± 1 cm^{-1} and I_D/I_G ratios between 0.95 ± 0.02 and 1.35 ± 0.02 were determined for the Spray ILGAR CuInS$_2$ thin films. In particular, variations of the G-mode position between 1577 ± 1 cm^{-1} and 1581 ± 1 cm^{-1} and of the I_D/I_G ratio between 1.02 ± 0.02 and 1.30 ± 0.02 were observed for

the same H$_2$S annealed Spray ILGAR CuInS$_2$ thin film (sample 420; Appendix I). This indicates that the fluctuations of both quantities within the same film are in the same range as the differences between different films. Therefore, the influence of the preparation parameters on the G-mode position and on the I_D/I_G ratio was not investigated any further. In Fig. 5.21, the G-mode positions and I_D/I_G ratios determined from the Spray ILGAR CuInS$_2$ thin films are shown together with the corresponding values for graphite, NC-G, a-C and ta-C according to the three-stage-model in Fig. 5.19 [Ferrari '04]. Additionally, the directions of increasing amorphization (black dashed arrows) and ordering (gray dotted arrows) are indicated.
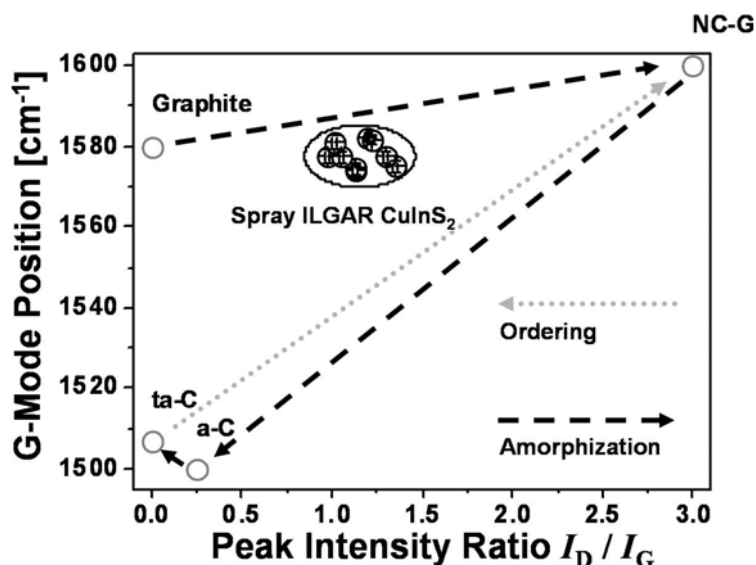

Fig. 5.21: G-mode positions and I_D/I_G ratios determined from the Raman spectra of Spray ILGAR CuInS$_2$ thin films (samples 329, 419, 420, 421; Appendix I). Additionally, the G-mode positions and I_D/I_G ratios for graphite, NC-G, a-C and ta-C according to the three-stage-model are given for an excitation wavelength of $\lambda = 633$ nm [Ferrari '04]. The directions of increasing amorphization are indicated by the black dashed arrows, whilst the direction of increasing ordering is indicated by the gray dotted arrow. The Raman spectra of the Spray ILGAR CuInS$_2$ thin films were obtained using an excitation wavelength of $\lambda = 633$ nm.

The comparison of the G-mode positions and I_D/I_G ratios determined from the Raman spectra of Spray ILGAR CuInS$_2$ in Fig. 5.21 with values for graphite, NC-graphite, a-C and ta-C reveals that the observed values for both quantities agree with the values expected for carbon materials in stage 1 or 2 of the three-stage-model (Fig. 5.19). Following this interpretation, the carbon in the Spray ILGAR CuInS$_2$ thin films is present either as clustered graphite (stage 1) or as disordered NC-G (stage 2) corresponding to a phase between NC-G and a-C. Taking the amorphous appearance of the carbon-containing interlayers into account that was observed in TEM measurements (Fig. 5.18), the second interpretation appears to be more likely. Therefore, it is proposed that the region of amorphous appearance consists of a-C, whilst the particles observed in the interlayers are interpreted as NC-G. According to this interpretation, the content of sp^3 carbon in the films can be estimated to be below 20 %. Furthermore, the scattering of the G-mode positions and the I_D/I_G ratios determined within the same sample indicate that the interlayers exhibit an inhomogeneous composition throughout the films.

It must be noted that ERDA measurements performed at a H$_2$S and KCN treated Spray ILGAR CuInS$_2$ (sample 413; Appendix I) detected about 1.5 ± 1 at. % of hydrogen, whilst the carbon content was determined as 5 ± 1 at. % (section 4.4.2.4.). Therefore, the interlayers may also contain some hydrogen.

The Raman measurements of this section were meant to elucidate the origin of the interlayers, which were assumed to stem from the hfac groups of the Cu(hfac)$_2$ compound used for the spraying solutions of the Spray ILGAR process (Fig. 3.1). The decomposition of hfac groups

in the copper CVD process using Cu(hfac)$_2$ was investigated by Parmeter [Parmeter '93]. He showed that the hfac groups decompose to elemental carbon in a temperature range of 327-577 °C. Therefore, the decomposition of hfac groups to elemental carbon in the Spray ILGAR process seems reasonable and is compatible with the Raman measurements.

Thus, in conclusion, the Raman measurements presented in this section indicate that the carbon-containing interlayers in the *layered bottom layer* of the Spray ILGAR CuInS$_2$ thin films consist of nanocrystalline graphite and amorphous carbon, which may also contain a certain, yet unknown, amount of hydrogen. This interpretation is in accordance with the growth model deduced in section 4.5. For a precise determination of the sp^2/sp^3 ratio and of the hydrogen content of these interlayers, complementary Raman measurements using various exciting wavelengths including UV excitation would be needed.

5.4. Origin of the Spectral Shape of the Chalcopyrite A$_1$ Mode in CuInS$_2$ Thin Films

If the Spray ILGAR CuInS$_2$ thin films are used as absorber layers in solar cells, most of the charge carrier separation will occur in the *well-crystallized top layer* of the absorber layers, since it is closest to the heterojunction. Therefore, the photovoltaic properties of the resulting devices can be expected to depend on the defect density in the *well-crystallized top layer*.

Thus, in this section, the structural defect density of the *well-crystallized top layer* of the Spray ILGAR CuInS$_2$ thin films is assessed by analyzing the spectral shape of the A$_1$ Raman mode of chalcopyrite-type CuInS$_2$, which is observed at a Raman shift of about 292 cm^{-1}. This mode corresponds to the vibration of the sulfur sublattice in the crystal lattice of chalcopyrite-type CuInS$_2$. In Fig. 5.22, the directions of the atomic movements of sulfur for this mode are indicated by the red arrows.
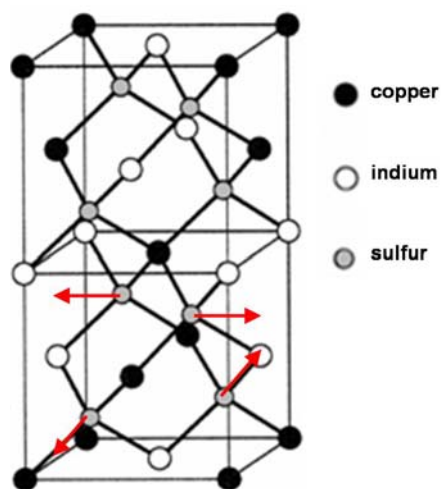

Fig. 5.22: Atomic movements of the sulfur atoms for the A$_1$ mode of chalcopyrite-type CuInS$_2$. For the sake of clarity, the movements are only indicated for the lower half of the crystal lattice. The sulfur atoms in the upper part vibrate analogously.

This mode exhibits an asymmetric shape in Spray ILGAR CuInS$_2$ thin films (red curve in Fig. 5.23). Variations of its peak position in the range of 1-2 cm^{-1} were also observed in the course of this work. Similar observations were reported by Rudigier [Rudigier '03], who investigated RTP-prepared CuInS$_2$ thin films (green curve in Fig. 5.23) and empirically found that the asymmetry is directly correlated to the photovoltaic performance of solar cells based on such films.

In section 5.4.1., the influence of strain on the Raman spectrum of the A$_1$ mode of chalcopyrite-type CuInS$_2$ is discussed.

The observed asymmetry of the A$_1$ mode of chalcopyrite-type CuInS$_2$ in Spray ILGAR CuInS$_2$ thin films is considered in section 5.4.2. A brief review is given over previous reports, focusing on the asymmetry of the same mode in RTP-processed CuInS$_2$ thin films [Rudigier

'03]. The spectral shape of this mode, as observed in Raman spectra obtained from single-crystalline, $CuInS_2$ samples is also discussed.

In section 5.4.3., the *phonon confinement model* (PCM) [Richter '81; Nemanich '81] is introduced, which will be applied to quantitatively describe the observed asymmetry of the A_1 mode of chalcopyrite-type $CuInS_2$ in the proceeding sections. This model correlates the spectral shape of Raman modes to domain sizes in the probed material. These may either correspond to distances between structural defects or to grain sizes.

Section 5.4.4. discusses extensions and modifications of the PCM that were made in the course of this thesis so that it could be applied to the Raman spectra of $CuInS_2$ thin films.

The modeling of the Raman spectra of the A_1 mode of chalcopyrite-type $CuInS_2$ obtained from Spray ILGAR and RTP-processed $CuInS_2$ thin films is described in section 5.4.5. and the results of this modeling are presented.

Finally, section 5.4.6. considers the physical relevance of the results obtained from the modeling of the Raman spectra of the A_1 mode of chalcopyrite-type $CuInS_2$ by comparing them with TEM measurements of Spray ILGAR and RTP-processed $CuInS_2$ thin films.
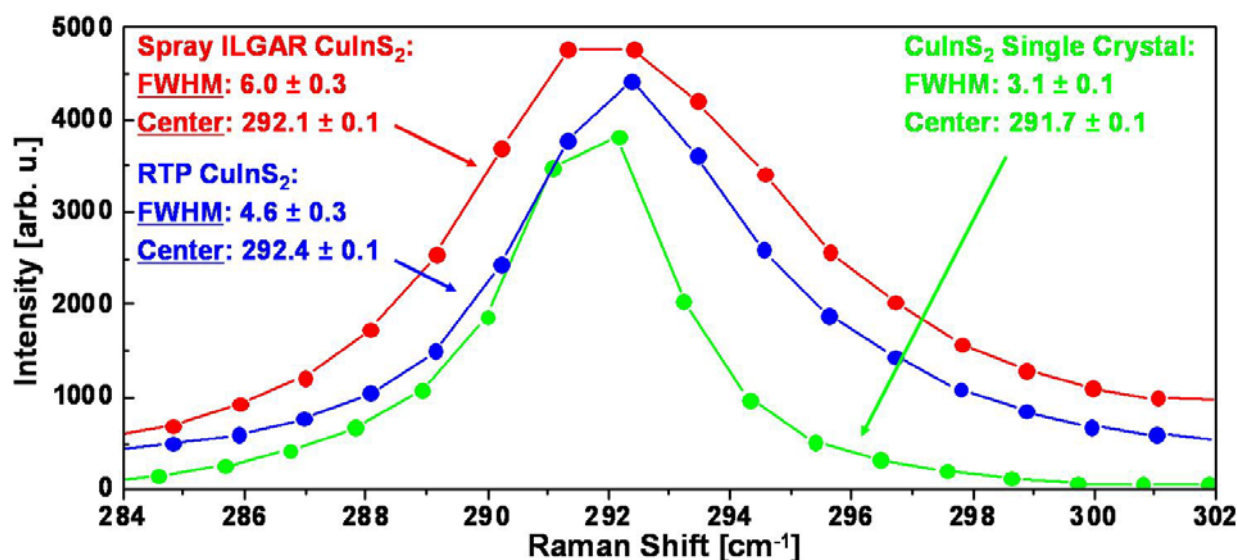

Fig. 5.23: Raman spectra of the A_1-mode (at about 292 cm⁻¹) of chalcopyrite-type $CuInS_2$ obtained from a Spray ILGAR (red upper trace), a RTP-processed (blue medium trace) $CuInS_2$ thin film and from a CVT-grown $CuInS_2$ single crystal (green lower trace). The spectra are shifted on the intensity scale for the sake of clarity. The *full width at half maximum* (FWHM) of the spectra and the peak center position is given for the spectra as determined by fitting the spectra with asymmetric (Spray ILGAR, RTP) and symmetric Lorentzians. The preparation parameters of the Spray ILGAR $CuInS_2$ thin film are given in Appendix I, whilst the RTP-$CuInS_2$ film was prepared according to the baseline process (section 2.2.) Both films were etched in KCN in order to remove copper sulfide phases from the film surface.

5.4.1. Influence of Strain on the A_1 Mode of $CuInS_2$

The position of a Raman line can be shifted due to strain present in the film. This is due to deviations in the interatomic spacings in the crystal lattice that are caused by the strain. These deviations result in changes of the vibrational frequencies of the lattice. For $CuInS_2$ the influence of strain on the Raman spectrum was investigated by Pinnick *et al.* [Pinnick '03], who performed Raman measurements at a $CuInS_2$ single crystal under hydrostatic pressure. These authors observed a blue shift of the spectrum for compressive pressure, which was not accompanied by any observable changes in the peak shape [Pinnick '03]. Additionally, Álvarez-García observed a redshift for RTP-processed $CuInS_2$ thin films, which showed a tensile strain [Álvarez Garcia_1 '02]. An empirical equation was introduced for the shift of the A_1-mode of $CuInS_2$ under hydrostatic pressure p by Pinnick *et al.* [Pinnick '03]:

$$\omega(A_1) = 290.9 \, \text{cm}^{-1} + p \times 5.17 \, \text{cm}^{-1} / \text{GPa} \qquad \text{Eq. (5.10a)}$$

thus, the pressure-induced shift is: $\Delta\omega(A_1) = p \times 5.17 \, \text{cm}^{-1} / \text{GPa}$ Eq. (5.10b)

5.4.2. Asymmetry of the A$_1$-mode in CuInS$_2$ Thin Films

In this section, the asymmetry of the A$_1$ Mode of chalcopyrite-type CuInS$_2$ is discussed. In Fig. 5.23, the Raman spectra of this mode obtained from such thin films are compared to a spectrum recorded on a CVT-grown CuInS$_2$ single crystal.

The Spray ILGAR CuInS$_2$ thin film was H$_2$S and KCN treated and had a *well-crystallized top layer* of a thickness of about 500-1000 nm (sample 421). Thus, the Raman spectra of this film can be assumed to only probe the *well-crystallized top layer* as it was desired. The preparation parameters of this film are given in Appendix I. The RTP CuInS$_2$ thin film, whose Raman spectrum is also shown in Fig. 5.23, was prepared according to the baseline process described in section 2.2. The stoichiometric CuInS$_2$ single crystal (25x3x2 mm^3) was free of strain (as indicated by Laue measurements [Schorr '07]) and may thus be regarded as a material reference. All Raman spectra, which are discussed in section 5.4., were obtained from these three samples.

It can be seen in Fig. 5.23 that the peak obtained from the single crystal shows a symmetric shape, whilst those of the Spray ILGAR and RTP CuInS$_2$ thin films are asymmetric such that they are broadened towards higher wavenumbers. For the single crystal spectrum in Fig 5.23, the A$_1$ mode of chalcopyrite-type CuInS$_2$ was observed at a Raman shift of 291.7 ± 0.1 cm^{-1}. The *full width at half maximum* (FWHM) of this peak was determined as 3.1 ± 0.1 cm^{-1}. In contrast, for the Spray ILGAR CuInS$_2$ Raman spectrum a peak position of 292.1 ± 0.1 cm^{-1} and a FWHM of 6.0 ± 0.3 cm^{-1} were obtained. The respective values for the RTP-processed film were 292.4 ± 0.1 cm^{-1} and a 4.6 ± 0.3 cm^{-1}, respectively. These values show that for both thin films, the peak positions as well as the asymmetrically broadened peak shape clearly deviate from the behavior of the single crystal.

Note that the asymmetric broadening is not related to the possible contribution of the A$_1$ mode of CuAu-ordered CuInS$_2$. The latter is observed at wavenumbers around 305 cm^{-1}. In Fig. 5.24a, a Spray ILGAR CuInS$_2$ Raman spectrum is shown, which was fitted by two Lorentzians. Even though the part of the spectrum related to CuAu-ordered CuInS$_2$ is well described by the fit, the chalcopyrite-related part around 292 cm^{-1} deviates from the fit. Therefore, Rudigier *et al.*, who firstly observed the asymmetric broadening of the A$_1$ mode of chalcopyrite-type CuInS$_2$ in RTP-prepared CuInS$_2$ thin films [Rudigier '03], used asymmetric Lorentzians for fitting the Raman spectra. The equation for an asymmetric Lorentzian is given in (Eq. (5.11)).

$$I(\omega) = \frac{I_0}{1 + 4\dfrac{\omega_t^2}{(\text{FWHM})^2}} \quad \text{with} \quad \omega_t = \frac{\omega - \omega_0}{1 - \xi \dfrac{\omega - \omega_0}{\text{FWHM}}} \qquad \text{[Rudigier '03]; Eq. (5.11)}$$

Here, I_0 is the peak intensity, ξ is the asymmetry value and ω_0 the position of the peak center. In Fig. 5.24b, the same spectrum shown in Fig. 5.24a was fitted with an asymmetric Lorentzian for the chalcopyrite peak. The contribution of CuAu-ordered CuInS$_2$ was fitted by a symmetric Lorentzian. Compared to the fit in Fig. 5.24a, the chalcopyrite-related part of the spectrum is well described. However, deviations are now observed at higher wavenumbers (>310 cm^{-1}) due to the slow decay of the asymmetric Lorentzian. Note that even though such peaks described the measured Raman spectra better than symmetric Lorentzians, this peak shape was chosen empirically and thus only allowed for a qualitative assessment of the spectra. For a quantitative analysis of the asymmetric broadening, possible mechanisms that can cause such a broadening have to be taken into account.
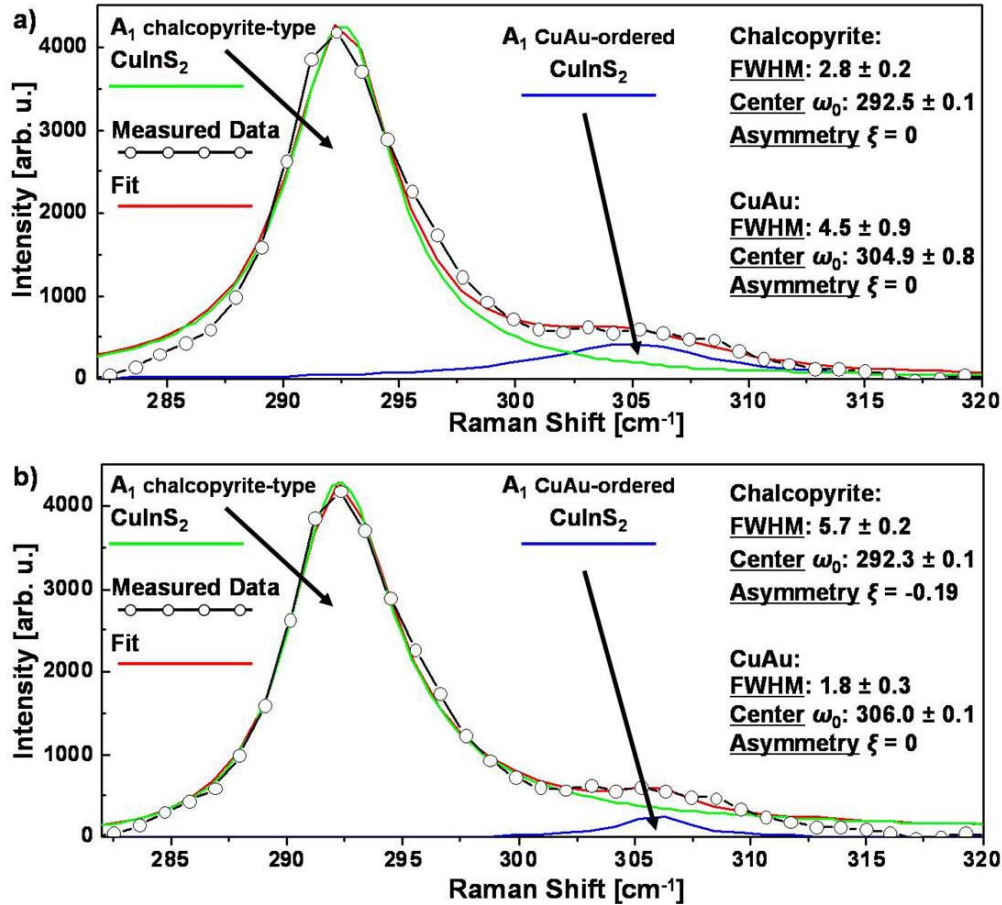
Fig. 5.24: Raman spectra of the A$_1$ Mode (at about 292 cm^{-1}) of chalcopyrite-type and CuAu-ordered (at about 305 cm^{-1}) CuInS$_2$ obtained from a Spray ILGAR (sample 421) CuInS$_2$ thin film. In (a), both modes were fitted using symmetric Lorentzians, whilst in (b), the chalcopyrite mode was fitted by an asymmetric Lorentzian (Eq. (5.11)). For the CuAu-order A1 mode a symmetric Lorentzian was used also in (b). The fit parameters for the peak center ω_0, FWHM and the asymmetry ξ are given in the figures. The preparation parameters of the Spray ILGAR CuInS$_2$ thin film are given in Appendix I.

Ideally, a Raman mode should be a delta-function centered at the Raman shift that correspond to the frequency of the respective oscillation of the lattice [Cardona '82; Yu '05]. In real Raman spectra, the Raman modes can usually be described by symmetric Lorentzians. This is a consequence of the finite lifetime of the excitation that causes the emission of the mode (Eq. 5.6) [Cardona '82; Yu '05]. In contrast, an asymmetric broadening results from a contribution of a collection of oscillators with a distribution of frequencies around the main frequency of the respective Raman mode. Such a contribution of oscillators with more than one frequency may have different reason, such as a real change of the vibrational properties in the probed material due to disorder in the crystal lattice or quantum mechanical effects, which are related to the confinement and uncertainty of the wave vector.

Rudigier *et al.*, qualitatively argued that the broadening of the A$_1$ Mode, may be attributed to an effect of the latter kind [Rudigier '03]. They suggested that the asymmetric broadening may be due to the confinement of phonons by crystallographic defects in the CuInS$_2$ thin films. The effect of phonon confinement in semiconductors, can be described quantitatively by the *phonon confinement model* (PCM), which was introduced by Richter *et al.* [Richter '81] and also by Nemanich *et al.* [Nemanich '81]. However, the applicability of the PCM to CuInS$_2$ thin films was not assessed quantitatively by Rudigier *et al.* In the following, such a quantitative analysis is performed for the first time.

5.4.3. The Phonon Confinement Model

The main idea behind the *phonon confinement model* (PCM), as it was introduced by Richter *et al.* [Richter '81] and by Nemanich *et al.* [Nemanich '81], is that as the symmetry of the crystal lattice is broken by the presence of crystallographic defects, also the $|q| \approx 0$ selection rule is relaxed in Raman spectroscopy. This means that as the scattering volume in the crystal becomes finite, i.e. the phonon is *confined* to a finite volume, also phonons of wavevectors q with $|q| > 0$ can contribute to the Raman spectrum. Depending on the slope of the phonon dispersion $\omega(q)$ of the Raman mode in the vicinity of the Γ-point (section 5.1.), the signal will become asymmetric and broaden either to the high energy side (positive slope) or the low energy side (negative slope).

Both, Richter *et al.* [Richter '81] and Nemanich *et al.* [Nemanich '81] proposed formalisms to describe this effect quantitatively. Thereby, Richter *et al.* followed a phenomenological approach to describe the Raman spectrum of nanocrystalline silicon [Richter '81], while Nemanich *et al.* deduced a structure factor $S(q)$ for the Raman scattering in nanocrystalline BN in analogy to the one used in X-ray diffraction theory [Nemanich '81]. Interestingly, both approaches yielded a mathematically similar formalism [Irmer '03; Gouadec '07; Irmer '07]. However, since the formalism introduced by Nemanich *et al.* does not include any arbitrarily chosen quantities, this approach is followed in this thesis. For a detailed comparison of both approaches, the reader is referred to Ref. [Irmer '03; Irmer '07].

The formalism proposed by Nemanich *et al.* [Nemanich '81] is based on the evaluation of the susceptibility function over a limited volume. This finally results in a proportionality relation for the spectral intensity distribution $I(\omega)$, i.e. the peak shape, of the Raman spectrum of a given Raman mode [Nemanich '81; Irmer '03; Irmer '07]:

$$I(\omega) \propto \iiint\limits_{\text{Brillouin zone}} \frac{S(q)}{(\omega - \omega(q))^2 - \dfrac{\Gamma^2}{4}} dq_x dq_y dq_z \qquad \text{Eq. (5.12)}$$

Here, ω is the frequency of the phonon and thus corresponds to the observed Raman shift. Γ and $\omega(q)$ are the natural linewidth and the phonon dispersion relation of the respective Raman mode. The integral in Eq. (5.12) is to be performed over the entire Brillouin zone. Thereby, the structure factor $S(q)$ acts as a weighing function and determines the contribution to the Raman spectrum of every phonon frequency ω along the phonon dispersion relation $\omega(q)$ as a function of the wavevector q. Generally, $S(q)$ is centered at $q = 0$, i.e. at the Γ-point of the Brillouin zone, and diminishes for $|q| > 0$. Its actual form depends on the geometry of the finite crystal volume, to which the phonons are confined. In Ref. [Irmer '03], $S(q)$ is given for various geometries. For the case of phonon confinement to spherical domains of a certain diameter L, $S(q)$ becomes:

$$S(q) = (9j_1^2(qL/2))/(qL/2)^2, \text{ where } j_1 \text{ is a spherical Bessel function} \qquad \text{Eq. (5.13)}$$

Substituting Eq. (5.13) into Eq. (5.12) yields:

$$I(\omega) \propto \iiint\limits_{\text{Brillouin zone}} \frac{\dfrac{9j_1^2(q\frac{L}{2})}{(q\frac{L}{2})^2}}{(\omega - \omega(q))^2 - \dfrac{\Gamma^2}{4}} dq_x dq_y dq_z \qquad \text{Eq. (5.14)}$$

Note that the lengths L obtained from the phonon confinement model do not necessarily correspond to a particle or grain size. They rather represent the typical distance between crystallographic defects in the probed material, which hinders the propagation of phonons in the crystal.

The expression in Eq. (5.14) can be simplified by an approximation introduced by Carles *et al.* [Carles '92]. Thereby, the phonon dispersion relation $\omega(\mathbf{q})$ is replaced by an averaged phonon dispersion $\omega_{ave}(q)$, which can be obtained by averaging over the various branches of the phonon dispersion relation $\omega(\mathbf{q})$ for different directions in the Brillouin zone [Carles '92]. Thereby, a possible degeneracy of these branches has to be taken into account [Carles '92]. By replacing $\omega(\mathbf{q})$ in Eq. (5.14) by $\omega_{ave}(q)$, the integral in Eq. (5.14) can be performed in one dimension from the Γ-point to a value, which corresponds to the radius of the Brillouin zone R_{BZ}. This corresponds to a transition from Cartesian to spherical coordinates, which leads to an additional factor of $4\pi q^2$ in the denominator. Thus, Eq. (5.15) is obtained:

$$I(\omega) \propto \int_{0}^{R_{BZ}} \frac{\dfrac{9 j_1^2(q\frac{L}{2})}{(q\frac{L}{2})^2} \cdot q^2}{(\omega - \omega_{ave}(q))^2 - \dfrac{\Gamma^2}{4}} dq \qquad \text{Eq. (5.15)}$$

The structure factor $S(q)$ for phonon confinement in spherical domains of diameter L (Eq. (5.13)) is shown for various values of L between 2 nm and 40 nm in Fig. 5.25.
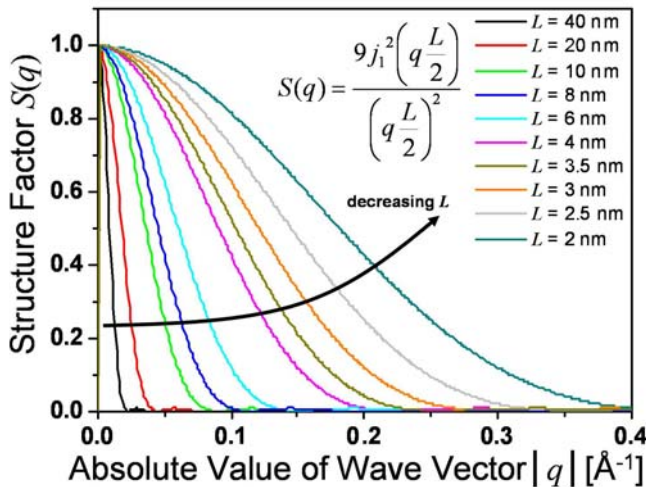

Fig. 5.25:   Structure factors (Eq. (5.13)) for phonon confinement in spherical domains of diameter L for different values of L according to the one-dimensional PCM (Eq. 5.15).

The structure factors in Fig. 5.25, all show a value of 1 at $|q| = 0$ and diminish as $|q|$ increases. In particular, the magnitude of $S(q)$ for a certain value of $q \neq 0$ increases for decreasing values of L, i.e. for phonon confinement in domains of decreasing size. Thus, the smaller the confining domains are, the higher is the contribution of phonons with $q \neq 0$ to the Raman spectrum. This can be understood as an increasing uncertainty of the wavevector q as the phonons are confined to domains of decreasing diameter L. This behavior qualitatively agrees with the behavior predicted by Heisenberg's uncertainty relation, which states that the product of the uncertainty in space and momentum of a given particle must equal or exceed a value of $\hbar/2$. The momentum of a phonon of wavevector q corresponds to a momentum of $\hbar \cdot q$, while its uncertainty in space is given by the diameter of the confining sphere L. Thus, the uncertainty relation requires that $\hbar \cdot \Delta q \cdot L \geq \hbar/2$ or $\Delta q \cdot L \geq 1/2$.

From Fig. 5.25, it can be seen, that $S(q) \approx 0$ for $|q| \cdot L/2 \approx 0.4$. The uncertainty of the wavevector q is thus $\Delta q = |q| \approx 3.2/L$ yielding $\Delta q \cdot L = 3.2$. Thus, the uncertainty exceeds the lower limit for the uncertainty of the wavevector q imposed by Heisenberg's uncertainty relation [Irmer '03; Irmer '07].

In the following, some limitations of the PCM are discussed, which have to be taken into account, when interpreting Raman spectra on the basis of this model.

Within the PCM it is assumed that the vibrational properties of the confining domains of a given material are equal to those of the infinite crystal. The only effect of the confinement

accounted for by the PCM is that the propagation of the phonons in the crystal is only allowed within these domain. Therefore, in the PCM formalism, the Brillouin zone and the phonon dispersion relation $\omega(\boldsymbol{q})$ of a given material are considered to be identical to those used for describing the bulk material. This has been justified by the fact that Raman spectroscopy is mainly sensitive to the local atomic structure in a material [Nemanich '05; Yu '05]. However, deviations of this behavior may be assumed to become significant as the domain size approaches the size of the unit cell of material.

Furthermore, it has to be taken into account that the PCM does not account for a size distribution of the confining domains, but only considers an average domain size. Additional effects, like scattering at the surface or boundaries of the confining domains, are also not included in the model. These effects may also contribute to the (asymmetric) broadening of a Raman mode [Nemanich '81]. Therefore, the domain sizes obtained from fits of Raman spectra according to the PCM can be considered to be a lower limit for the actual size of the confining domains. However, the PCM has been successfully used to determine or confirm particle sizes or defect densities from the Raman spectra of various nanocrystalline materials. Reviews about the application of the PCM and additional models are given in Ref. [Arora '03; Irmer '03; Gouadec '07; Irmer '07].

5.4.4. Modifications of the Phonon Confinement Model Formalism

In this section, it is described how the PCM formalism was adapted and extended in the course of this thesis, to simulate the spectral shape of the Raman A$_1$ mode of chalcopyrite-type CuInS$_2$ as obtained from Spray ILGAR and RTP-processed CuInS$_2$ thin films as well as from single-crystalline CuInS$_2$ according to the PCM.

As shown in section 5.4.1., strain, which may be present in the CuInS$_2$ thin films, may lead to a shift in the Raman spectrum of these films (Eq. (5.10)). However, a shift in the Raman spectrum would also be expected to accompany an asymmetric broadening, which is caused by phonon confinement [Nemanich '81]. In order to separate these two shifts, the PCM formalism was extended in the present work by entering an additional parameter C_{Strain} into the denominator of Eq. (5.15), which accounts for the strain-induced shift. This parameter, C_{Strain}, allows lateral variation of the position of a simulated Raman spectrum along the frequency axis (ω), independently of the actual PCM simulation of the peak shape. Thus, the equation to describe the PCM becomes:

$$I(\omega) \propto \int_{0}^{R_{BZ}} \frac{\dfrac{9\,j_1^2(q\frac{L}{2})}{(q\frac{L}{2})^2}\cdot q^2}{(\omega - C_{Strain} - \omega_{ave}(q))^2 - \dfrac{\Gamma^2}{4}}\,dq \qquad\qquad \text{Eq. (5.16)}$$

After the simulation of a Raman spectrum, the strain can be obtained from C_{Strain} by applying Eq. (5.10), as $C_{Strain} = p \times 5.17$ cm^{-1}/Gpa. This, however, only assumes a homogeneous strain distribution and does not account for depth dependent strain gradients.

In order to use Eq. (5.16) for simulating Raman spectra for the A$_1$ mode of chalcopyrite-type CuInS$_2$ according to the PCM, the phonon dispersion relation must be included in Eq. (5.16). The phonon dispersion relation of chalcopyrite-type CuInS$_2$ was calculated by Łazewski *et al.* for different directions in the Brillouin zone (ΓX, ΓN, PX, NP and ΓZ) using density functional theory [Lazewski '02]. This phonon dispersion as calculated by Łazewski *et al.* is shown in Fig. 5.26a, whilst the Brillouin zone of chalcopyrite-type CuInS$_2$ with the high symmetry points Γ, X, P, N and P is shown in Fig. 5.26b.
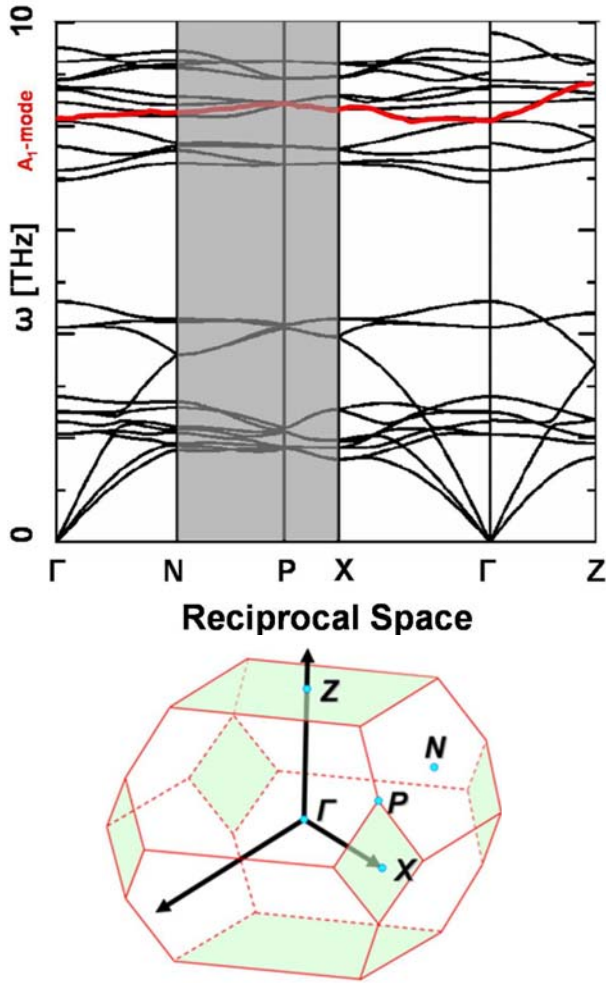
Fig. 5.26a: Phonon dispersion relation for the lattice vibrations of CuInS$_2$ as calculated by Łazewski *et al.* [Lazewski '02] using density functional theory for different directions in the Brillouin zone of chalcopyrite-type CuInS$_2$. The red curve indicates the dispersion of the A$_1$-mode. The gray-shaded areas have been neglected for the fits of the Raman spectra according to the PCM. The original image of the Dispersion relation was taken from Ref. [Lazewski '02] and modified for the present thesis.

Fig. 5.26b: Brillouin zone of chalcopyrite-type CuInS$_2$. The high symmetry points Γ, X, P, N and P are indicated. The Brillouin zone was redrawn from Ref. [Alonso '01].

In order to include The phonon dispersion relation of the A$_1$ mode of chalcopyrite-type CuInS$_2$ in Eq. (5.16), it was read out of Ref. [Lazewski '02] (Fig. 5.26a; indicated in red) for the branches ΓX, ΓN and ΓZ. The contribution of the branches PX and NP (gray-shaded area in Fig. 5.26a) to the Raman spectrum can be expected to be negligible compared to the contribution of the branches ΓX, ΓN and ΓZ, since the branches PX and NP are located on the edge of the Brillouin zone. Due to the decay of the structure factor $S(q)$ (Fig. 5.25) from the Γ-point towards the edges of the Brillouin zone, this can be expected to lead to a minor contribution of these branches.

For the same reason another simplification can be made: The lengths of the ΓX, ΓN and ΓZ branches are different in reciprocal space (Fig. 5.26b). Therefore, phonon dispersion relation of the A$_1$ mode of chalcopyrite-type CuInS$_2$ was approximated by averaging over those parts of the phonon dispersion relation branches ΓX, ΓN and ΓZ, which lay within a sphere, whose radius corresponds to the "length" of the shortest branch (ΓZ) of the phonon dispersion relation. This approximation is indicated by the blue sphere in Fig. 5.27. The "length" of the ΓZ branch corresponds to $|ΓZ| \approx π \cdot 0.0899$ Å$^{-1} \approx 0.2824$ Å^{-1} in reciprocal space [Alonso '01; Lazewski '02]. Inside this sphere, the phonon dispersion relation was approximated by an isotropic phonon dispersion relation $\omega_{ave}(q)$, which was obtained by averaging of the phonon dispersion relation along the branches ΓX, ΓN and ΓZ following the approach of Carles *et al.* [Carles '92], which was discussed above (section 5.4.3.). The parts of the phonon dispersion relation branches ΓX and ΓN that lay outside of this sphere were neglected. Again, it can be expected that these parts only minorily contribute to the Raman spectrum of the A$_1$ mode of chalcopyrite-type CuInS$_2$, as they are close to the edge of the Brillouin zone, where the weighting structure factor $S(q)$ exhibits its minimum values (Fig. 5.25). However, from the structure factors shown in Fig. 5.25, it can be seen that the wavevectors of the Brillouin zone

with $|q| > |\Gamma Z| \approx \pi\cdot 0.0899$ Å^{-1} ≈ 0.2824 Å^{-1} start to contribute to the Raman spectrum (meaning $S(q) \neq 0$), if the diameter L of the spherical confining domains becomes smaller than 2.5 nm. This means that then the approximations described in this paragraph start to become non-negligible, which has to be taken into account for the evaluation of simulated Raman spectra.
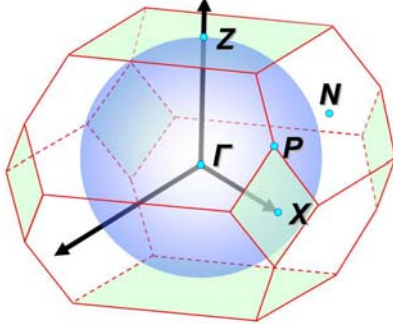

Fig. 5.27: Brillouin zone of chalcopyrite-type CuInS$_2$. The high symmetry points Γ, X, P, N and P are indicated. The Brillouin zone was redrawn from Ref. [Alonso '01]. The phonon dispersion relation of the A$_1$ mode of chalcopyrite-type CuInS$_2$ was approximated by averaging over the parts of the phonon dispersion relation branches ΓX, ΓN and ΓZ within the blue sphere, which has a radius that corresponds to the distance $|\Gamma Z| \approx \pi\cdot 0.0899$ Å$^{-1} \approx 0.2824$ Å^{-1} [Alonso '01; Lazewski '02]. The parts of the phonon dispersion relation branches ΓX and ΓN outside of the sphere were neglected.

In Fig. 5.28, this one-dimensional averaged isotropic phonon dispersion relation $\omega_{ave}(q)$, as obtained from the data reported in Ref. [Lazewski '02], is shown as a function of $|q|$, i.e. of the distance from the Γ-point for $0 \leq |q| \leq |\Gamma Z| \approx \pi\cdot 0.0899$ Å$^{-1} \approx 0.2824$ Å^{-1}.
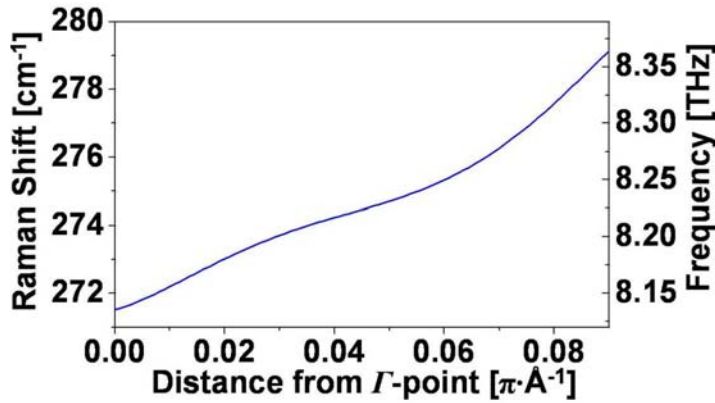

Fig. 5.28: Averaged one-dimensional phonon dispersion relation as it was derived from the phonon dispersion branches ΓX, ΓN and ΓZ of the A$_1$-mode of chalcopyrite-type CuInS$_2$, which are shown in Fig. 5.26a, $0 \leq |q| \leq |\Gamma Z| \approx \pi\cdot 0.0899$ Å$^{-1} \approx 0.2824$ Å^{-1}, which correspond to the radius of the blue sphere in Fig. 5.27 the edge of the Brillouin zone.

The calculated frequency in Ref. [Lazewski '02] of the A$_1$-mode of chalcopyrite-type CuInS$_2$ at the Γ-point of 8.14 THz corresponds to a Raman shift of $\omega = 271.52$ cm^{-1}. This value is significantly lower than those reported for CuInS$_2$ by various authors [Koschel_1 '75; Riedle '02; Rudigier '03; Rudigier '05], who all reported a Raman shift of about 292 cm^{-1}. This corresponds to a relative error of about 10 % for the density functional theory-calculated values. Even though this lies in an acceptable range for an ab-initio method like density functional theory, the deviation from the observed Raman shifts is too pronounced to use this calculated phonon dispersion relation for simulating a peak broadening, which is in the range of 1-2 cm^{-1}. However, for the peak fitting procedure the slope of the phonon dispersion is much more important than the actual peak position. Therefore, the averaged phonon dispersion was corrected by adding a constant value of 0.634 THz ($C_{corr} = 20.18$ cm^{-1}), so that the frequency at the Γ-point corresponded to the peak position of $\omega = 291.70 \pm 0.02$ cm^{-1} that was obtained from the CuInS$_2$ single crystal, which was described at the beginning of this section (Fig. 5.23).

This crystal was also used to approximate the natural line width Γ of the A$_1$-mode of chalcopyrite-type CuInS$_2$ in Eq. (5.16) by the FWHM of the single crystal Raman spectrum of 3.04 ± 0.05 cm^{-1}. Both values were obtained by averaging over the peak center positions and FWHM values, which were obtained from seven measurements recorded at different spots on the single crystal. By using these values and the averaged phonon dispersion relation (Fig. 5.28), Eq. (5.16) becomes:

$$I(\omega) \propto \int\limits_{0}^{0.2824} \frac{\dfrac{9 j_1^2(q\frac{L}{2})}{(q\frac{L}{2})^2} \cdot q^2}{(\omega - C_{\text{Strain}} - 20.18 - \omega_{\text{ave}}(q))^2 - \dfrac{3.04^2}{4}} dq \qquad \text{Eq. (5.17)}$$

Even though all Raman spectra investigated in this section are dominated by the contribution of the A$_1$ mode of chalcopyrite-type CuInS$_2$, a small additional contribution, which can be attributed to a contribution of the A$_1$ mode of CuAu-ordered CuInS$_2$ was also observed in some of the spectra (e.g. Fig. 5.24).

In order to simulate the measured Raman spectra and to obtain values for L and C_{Strain}, the presence of a contribution of CuAu-ordered CuInS$_2$ to the Raman spectrum has to be taken into account, if observable. Even though it has been shown that this mode is not the origin of the asymmetry of the A$_1$ mode of chalcopyrite-type CuInS$_2$ (Fig. 5.24), it still influences the simulation of the Raman spectra due to a partial overlap of both modes.

In order to reduce the number of free parameters in the equation used for the simulation of the Raman spectra, the position of the A$_1$ mode of CuAu-ordered CuInS$_2$ was determined in a *separate* fit. In this fit, the A$_1$-mode of chalcopyrite-type CuInS$_2$ was approximated by an asymmetric Lorentzian (Eq. (5.11)), whilst the A$_1$-mode of CuAu-ordered CuInS$_2$ was fitted by a symmetric Lorentzian[24] (compare Fig. 5.24b). The peak position of the A$_1$-mode of CuAu-ordered CuInS$_2$ was then used for the subsequent simulation of the Raman spectrum according to the PCM. In this simulation, a contribution of the A$_1$-mode of CuAu-ordered CuInS$_2$ to the Raman spectrum was accounted for by adding a standard Lorentzian to Eq. (5.17) at *this fixed peak position* ω_{CuAu}. The intensity and the FWHM of this peak were additional free parameters, which were varied during simulation in order to approximate the measured Raman spectrum. Additionally, the proportionality relation in Eq. (5.17) was turned into an equation by entering a proportionality factor I_0 that accounts for the intensity of the simulated spectrum. I_0 was also varied as a free parameter in the simulations. Thus, the final equation that was used for the fits of the Raman spectra was:

$$I(\omega) = I_0 \cdot \int\limits_{0}^{0.2824} \frac{\dfrac{9 j_1^2(q\frac{L}{2})}{(q\frac{L}{2})^2} \cdot q^2}{(\omega - C_{\text{Strain}} - 20.18 - \omega_{\text{ave}}(q))^2 - \dfrac{3.04^2}{4}} dq + \frac{I_{\text{CuAu}}}{1 + 4\dfrac{(\omega - \omega_{\text{CuAu}})^2}{(FWHM_{\text{CuA}})^2}} \qquad \text{Eq. (5.18)}$$

In Eq. (5.18) only I_0 (intensity of the A$_1$ mode of chalcopyrite-type CuInS$_2$), C_{Strain} (strain-induced peak shift), I_{CuAu} (intensity of the A$_1$ mode of CuAu-ordered CuInS$_2$) and $FWHM_{\text{CuAu}}$ (FWHM of the A$_1$ mode of CuAu-ordered CuInS$_2$) were free parameters, which were varied in the simulation in order to approximate the measured Raman spectra. The peak center position of the A$_1$ mode of CuAu-ordered CuInS$_2$ ω_{CuAu} was entered as a fixed parameter.

5.4.5. Modeling of Raman Spectra of the A$_1$ Mode of CuInS$_2$

In this section, the Raman spectra of the A$_1$ mode of chalcopyrite-type CuInS$_2$ obtained from a Spray ILGAR CuInS$_2$ thin film, a RTP-processed CuInS$_2$ thin film and a CVT-grown CuInS$_2$ single crystal are modeled according to the PCM formalism (Eq. 5.18) that was described in section 5.4.4.

---

[24] Even though an asymmetric shape of the A$_1$-mode of CuAu-ordered CuInS$_2$ might be possible, this procedure should cause only a negligible error, since only such Raman spectra were investigated in this section, in which the contribution of the A$_1$ mode of CuAu-ordered CuInS$_2$ was significantly lower than that of the A$_1$ mode of chalcopyrite-type CuInS$_2$. See also Table 5.4 in section 5.4.5.

The preparation of the samples has been described in the introduction of this section. In the following, seven Raman spectra obtained at seven arbitrarily chosen spots (diameter 1-2 μm) on each of these samples were approximated by simulated Raman spectra according to the PCM (Eq. 5.18). Each of the spectra has been corrected for a linear background and for a thermal shift of the spectrometer as described in section 5.1.4. (Fig. 5.4).

In order to simulate the measured Raman spectra according to the PCM (Eq. 5.18), a numerical simulation routine was written using Mathcad™ [MathSoft '01]. The code of this routine is given in Appendix VI. This routine simulated the measured Raman spectra by performing a mean-least-squares fit of the spectrum. The same routine could also be used to generate simulated Raman peaks according to the PCM on the basis of Eq. (5.18) without the input of a measured spectrum. In Fig. 5.29, simulated Raman spectra of the A$_1$ mode of chalcopyrite-type CuInS$_2$ are shown for different values of the diameter L of the spherical domains, to which the phonons are confined according to the PCM. For the simulated spectra in Fig. 5.29, C_{Strain} and I_{CuAu} in Eq. (5.18) were set to zero meaning that the spectra represent unstrained single-phase chalcopyrite CuInS$_2$.
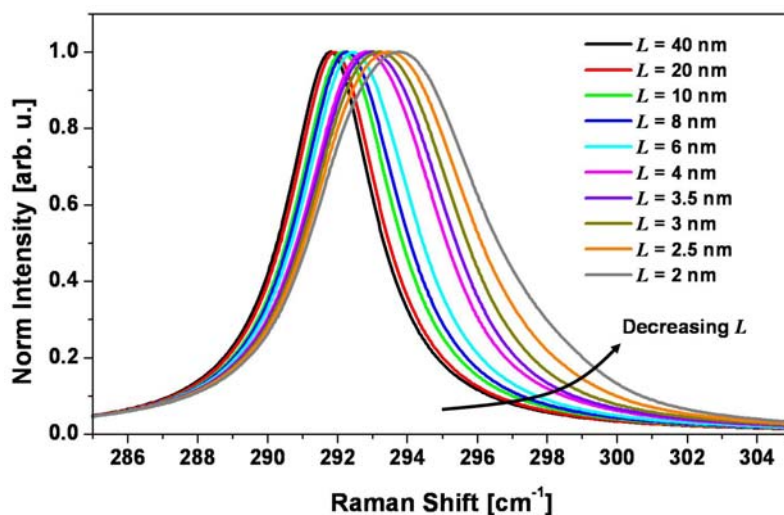

Fig. 5.29: Simulated Raman spectra of the A$_1$ mode of chalcopyrite-type CuInS$_2$ obtained from Eq. (5.18) for different values of the diameter L of spherical domains, to which the phonons of this mode are confined according to the PCM. For these spectra, C_{Strain} and I_{CuAu} were set to zero, i.e. no strain or contribution of CuAu-ordered CuInS$_2$ is considered.

From the simulated spectra in Fig. 5.29, the influence of the phonon confinement on the spectral shape of the A$_1$ mode of chalcopyrite-type CuInS$_2$ becomes clear. As the diameter of the confining spherical domains decreases from $L = 40$ nm to $L = 2$ nm, the peak broadens asymmetrically and shifts towards higher wavenumbers. It was argued above that for $L < 2.5$ nm, the $S(q)$ already reaches non-zero values at the edge of the Brillouin zone in the ΓZ direction. Thus, the approximated one-dimensional phonon dispersion relation in Fig. 5.28 becomes inaccurate for $L < 2.5$ nm. Additionally, a diameter L of the confining spheres of 2.5 nm roughly corresponds to twice the size of the unit cell of chalcopyrite-type CuInS$_2$. Hence, the assumption of the PCM that the confining domains exhibit the same properties as the bulk crystal may not be valid anymore. Therefore, the physical relevance of values of L below 2.5 nm becomes questionable.

In the following, the approximation of measured Raman spectra by spectra simulated according to the PCM (Eq. 5.18) are discussed. Furthermore, the values for the strains p and the diameters of the confining domains L obtained from these spectra, are assessed.

In Fig. 5.30a, representative Raman spectra (symbols) of the A$_1$-modes of a H$_2$S and KCN treated Spray ILGAR CuInS$_2$ thin film (black stars), a KCN etched RTP-processed CuInS$_2$ thin film (red triangles) and of the CuInS$_2$ single crystal (blue circles) are shown.
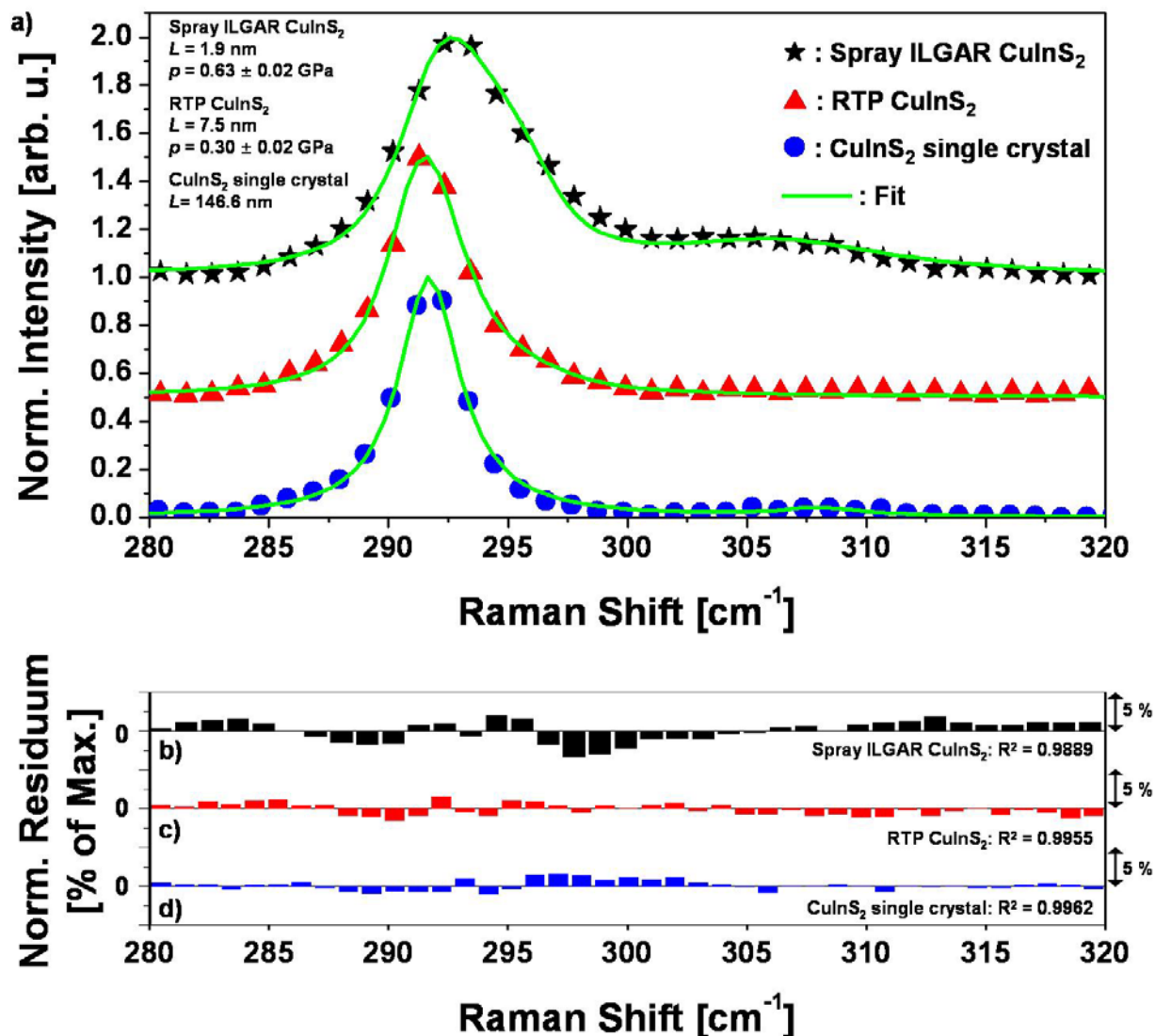
Fig. 5.30: a) Measured (symbols) and simulated (red lines) Raman spectra of a Spray ILGAR CuInS$_2$ thin film (sample 421), an RTP-processed CuInS$_2$ thin film and a CuInS$_2$ single crystal. The values for the diameter of the confining spherical domains L and the strains p that were determined from the fits are stated. No strain is stated for the single crystal, since it served as an unstrained reference. The measured spectra were approximated by simulated spectra according to Eq. (5.18). The spectra are shifted with respect to each other on the y-axis for the sake of clarity. Prior to the fits the spectra were corrected by subtracting a linear background. b)-d) Residuals of the fits in a). Additionally, the coefficient of determination R^2 (Appendix VI; Eq. (VI.1)) of the fits is stated.

Clear differences between the three spectra are visible. The peaks of the polycrystalline Spray ILGAR and RTP CuInS$_2$ thin films reveal an asymmetric broadening, which is most pronounced for the Spray ILGAR film. In contrast, no asymmetry is observed for the CuInS$_2$ single crystal peak. Also, the maxima of the spectra vary by about 1-2 cm^{-1}. In the spectra of the Spray ILGAR CuInS$_2$ film, the peak of the A$_1$-mode of CuAu-ordered CuInS$_2$ appears around 305 cm^{-1}. A very weak contribution of this peak is also observed in the single crystal spectrum, whereas no CuAu-ordered CuInS$_2$ is observed in the spectrum of the RTP-CuInS$_2$ film. However, in some of the spectra of the RTP-processed CuInS$_2$ film a small contribution of CuAu-ordered CuInS$_2$ was observed. In addition, the fits of these Raman spectra with simulated spectra according to the PCM (Eq. (5.18)) are also shown (green lines) in Fig. 5.30a. It can be seen that the simulated spectra describe the measured spectra well, which can also be seen from the residuals (Fig. 5.30b-d) and the *coefficients of determination R^2* of the

fits (Appendix VI; Eq. (VI.1); $R^2 \approx 0.99$ for all three fits). This is a first indication that the asymmetric peak broadening of the A$_1$-mode is indeed caused by phonon confinement.

From the fits in Fig. 5.30a, values for the diameters L of the confining spherical domains of L = 1.9 nm (Spray ILGAR CuInS$_2$), L = 7.5 nm (RTP-CuInS$_2$) and L = 146.6 nm (CuInS$_2$ single crystal) were obtained[25]. The strains p for the CuInS$_2$ thin films were tensile and were determined as p = 0.63 ± 0.02 GPa (Spray ILGAR CuInS$_2$) and p = 0.30 ± 0.02 GPa (RTP-CuInS$_2$) from the fits in Fig 5.30a. Since the CuInS$_2$ single crystal served as an unstrained material reference, no strain was obtained for this sample. In Table 5.4, the values for the diameters of the confining spherical domains L and strains p, which were obtained by approximating all seven measurements recorded on each of the three samples by simulated spectra according to Eq. (5.18), are listed together with the R^2-values of the fits.

Mean values for the diameters L of the confining spherical domains, which were obtained from the simulated spectra of the seven measurements performed on each sample, were determined as L = 1.7 ± 0.2 nm for Spray ILGAR CuInS$_2$, L = 7.1 ± 5.8 nm for RTP-CuInS$_2$ and L = 146.2 ± 2.1 nm for the single crystal. The stated uncertainties reflect the standard deviations of the measurements.

The mean diameter L of the confining spherical domains determined for the CuInS$_2$ single crystal of 146.2 ± 2.1 nm greatly exceeds the values, which were deduced for the polycrystalline thin films, as it was expected for the comparison of a single crystal with polycrystalline thin films

The assessment of the diameters L of the confining spherical domains obtained from the simulated Raman spectra of the Spray ILGAR CuInS$_2$ thin film show that all of the values for L are below the critical value of L = 2.5 nm, which corresponds to a decay of the weighting structure factor $S(q)$ to about zero at $|q| = |\Gamma Z| \approx 0.2824$ Å^{-1}. Therefore, the physical relevance of the absolute values of L obtained from the simulated Raman spectra for the Spray ILGAR CuInS$_2$ thin film is questionable. However, the simulated spectra still approximated the measured spectra quite well in most cases (spectra #2-#7), which is reflected by the coefficients of determination R^2 that exceeded a value of 0.97 for all spectra except spectrum #1. Hence, the obtained values of L for the Raman spectra of this film may be interpreted such that the peak shape of these spectra may be attributed to phonon confinement and the diameter L of the confining spherical domains must be smaller than the critical value of 2.5 nm. Generally, the simulated spectra described the measured spectra well, if the spectra exhibited only minor contributions of CuAu-ordered CuInS$_2$. The smallest values of R^2 were obtained for spectra #1 and #3 (Table 5.4), which showed the strongest contributions of the A$_1$ mode of CuAu-ordered CuInS$_2$ of all investigated spectra, (peak area ratios of the A$_1$ modes of chalcopyrite-type and CuAu-ordered CuInS$_2$ of 2.4 and 5.5 using the fitting procedure described in section 5.4.4.). It may be assumed that in these cases the influence of the A$_1$ mode of CuAu-ordered CuInS$_2$ was too strong to be accounted for completely by Eq. (5.18). The strong contribution of CuAu-ordered CuInS$_2$ to these spectra might be caused by local fluctuations of the thickness of the *well-crystallized top layer* of the Spray ILGAR CuInS$_2$ thin film.

For the RTP-processed CuInS$_2$ thin film, the approximation of the Raman spectra by simulated spectra according to the PCM (Eq. (5.18)) yielded values L for the diameters of the confining spherical domains above the critical value of 2.5 nm for all but one spectra. For this spectrum, a value of L = 2.3 nm was obtained, which is only slightly below the critical value. Therefore, the obtained values for L can be assumed to be physically relevant. For the spectrum for which L = 2.3 nm was obtained, the same argumentation holds as for the Spray ILGAR spectra. The peak shape may be attributed to the PCM and the diameter of the confining spherical domains must be smaller than 2.5 nm.

---

[25] The uncertainties of the derived values for L are discussed at the end of this section.

Table 5.4:   Values resulting from the fitting of the measured Raman spectra according to the PCM (Eq. (5.18)). Values for the diameters L of the confining spherical domain$s$, the standard deviation of L σ_L in the respective sample, the tensile strains p, the standard deviation of p σ_p in the respective sample, the peak area ratio of the A$_1$ Modes of chalcopyrite-type and CuAu-ordered CuInS$_2$, as well as the R^2-value of the fits are listed. The bold lines indicate the mean values for the respective sample. The preparation parameters for the Spray ILGAR CuInS$_2$ thin film (sample 421) are listed in Appendix I. The RTP-processed CuInS$_2$ thin film was prepared according to the baseline process for CuInS$_2$ (section 2.2). The single crystal was prepared by CVT.

	L [nm]	σ_L[nm]	p[GPa]	σ_p[GPa]	Area Ratio Chalcopyrite:CuAu	R^2
\<RTP CuInS$_2$\>	**7.1**	**5.8**	**0.33**	**0.13**	/	/
RTP #1	5.0	/	0.48	/	∞	0.9928
RTP #2	5.2	/	0.33	/	26.8	0.9974
RTP #3	5.0	/	0.31	/	87.0	0.9955
RTP #4	19.8	/	0.14	/	67.9	0.9972
RTP #5	2.3	/	0.52	/	27.6	0.9930
RTP #6	7.5	/	0.30	/	∞	0.9955
RTP #7	5.0	/	0.26	/	66.9	0.9918
\<Single crystal\>	**146.2**	**2.1**	/	/	/	/
Single crystal #1	146.3	/	/	/	12.3	0.9999
Single crystal #2	146.2	/	/	/	15.6	0.9954
Single crystal #3	148.8	/	/	/	17.7	0.9951
Single crystal #4	146.6	/	/	/	16.0	0.9962
Single crystal #5	146.7	/	/	/	9.9	0.9958
Single crystal #6	142.0	/	/	/	13.7	0.9952
Single crystal #7	146.9	/	/	/	16.2	0.9935
\<ILGAR CuInS$_2$\>	**1.7**	**0.2**	**0.62**	**0.05**	/	/
ILGAR CuInS$_2$ #1	1.4	/	0.64	/	2.4	0.9397
ILGAR CuInS$_2$ #2	1.7	/	0.62	/	8.5	0.9799
ILGAR CuInS$_2$ #3	1.6	/	0.60	/	5.5	0.9703
ILGAR CuInS$_2$ #4	1.9	/	0.63	/	28.3	0.9889
ILGAR CuInS$_2$ #5	1.8	/	0.63	/	19.0	0.9849
ILGAR CuInS$_2$ #6	1.9	/	0.53	/	16.4	0.9899
ILGAR CuInS$_2$ #7	1.7	/	0.71	/	119.9	0.9882

Generally, the obtained domain diameters are about two to three orders of magnitudes smaller than the grain sizes observed for the same kind of films by SEM (Fig. 4.18e) [Abou-Ras '07]. Thus, the confinement must be caused by subgrain defects, if the asymmetric peak broadening is caused by the confinement of phonons. What kind of defect could account for the confinement will be discussed in the following section.

According to the PCM, the observation that the L values of the RTP-processed CuInS$_2$ thin films exceed those obtained for the Spray ILGAR CuInS$_2$ thin films, means that the density of crystallographic defects in the Spray ILGAR CuInS$_2$ thin films exceeds that of the RTP-processed film. From the mean values obtained from the simulated Raman spectra the density of crystallographic defects, may be estimated to be of the order of 10^{19} cm^{-3} for the RTP-processed CuInS$_2$ thin films. For the single crystal a value of 10^{15} cm^{-3} follows from the mean L value in Table 5.4. For the Spray ILGAR CuInS^2 thin film, the defect density should be higher than 10^{20} cm^{-3}.

Approximating the Raman spectra measured on the Spray ILGAR and the RTP CuInS$_2$ films by simulated spectra according to Eq. (5.18), yielded tensile strains for all spectra investigated in this section. For the RTP-CuInS$_2$ thin film, a mean tensile strain of $p = 0.33 \pm 0.13$ GPa was determined. The mean value for the Spray ILGAR CuInS$_2$ film was $p = 0.62 \pm 0.05$ GPa. Since the peak shape of the measured Raman spectra could be described quite well by Eq. (5.18) for all investigated spectra, the obtained values for the strains p may be expected to be physically relevant.

RTP-CuInS$_2$ thin films, which were processed identically to the ones investigated in this

section, have also been investigated by Álvarez-García [Álvarez Garcia_1 '02] using X-ray diffraction. Thereby, he determined a tensile strain of $p = 0.17 \pm 0.06$ GPa. Even though this value for p lies slightly below the mean value obtained from the simulated Raman spectra according to Eq. (5.18), both values still overlap with in their margins of deviation. This indicates the validity of the approach used in this section for approximating the measured Raman spectra.

Uncertainties of the Strains p and the Diameters of the Confining Spherical Domains L

As discussed above, the influence of the phonon confinement and strain on the Raman spectrum are different. While strain causes a shift of the peak without an observable change of its shape (assuming a homogeneous strain distribution; section 5.4.1.), the phonon confinement influences both, the position of the peak maximum and the shape of the peak (Fig. 5.29). Thus, the uncertainty of the strain can be obtained from the uncertainty of the peak position, i.e. of the calibration of the Raman shift axis (Fig. 5.4). Using Eq. (5.10), this yielded an uncertainty of $\Delta p = \pm 0.02$ GPa for the strain value obtained from a single fit. However, the scattering of the strain values obtained from measurements at different points of the same film was found to exceed this uncertainty. This indicates a local variation of the strains in the films, which seems reasonable for polycrystalline films.

The estimation of the uncertainty of the obtained values for the diameters L of the confining spherical domains is more complicated. Eq. (5.18), used for fitting the spectra, has been derived from the PCM. This model is based on quantum mechanical considerations and includes several simplifications [Nemanich '81]. The most important simplification is that the PCM assumes that the phonons are confined to *spheres* of perfect crystalline order. In reality, the crystallographic defects that cause the confinement can be expected to be distributed statistically. Additionally, the phonon dispersion relation used in Eq. (5.18) was calculated by density functional theory. Therefore, nothing is known about its uncertainty. Finally, the uncertainties of the derived diameters L of the confining spherical domains depend on the goodness of the approximation of the measured spectrum by the simulated one. This goodness is reflected by the *coefficient of determination R^2* ($0 \leq R^2 \leq 1$; Appendix VI; Eq. (VI.1)), which is stated in Table 5.4. for each spectrum. It can be seen that for all single crystal and RTP CuInS$_2$ spectra approximations, values of $R^2 \geq 0.99$ were obtained. For the approximated Spray ILGAR CuInS$_2$ values of $R^2 \geq 0.98$ were obtained for spectra #4-#7, whilst for the Spray ILGAR spectra #1, #2 and #3 R^2 was smaller than 0.98. Furthermore, the diameters of the confining spherical domains and strains derived from spectra, which were obtained on the same sample only scattered in a relatively narrow range (1.4-1.9 nm for Spray ILGAR CuInS$_2$, 2.3-19.8 nm for RTP-CuInS$_2$ and 142.0-148.8 nm for the single crystal). These values indicate that – at least for the RTP and single crystalline CuInS$_2$ – the uncertainty originating from the goodness of the fits is small compared to that arising from a possible uncertainty of the phonon dispersion relation. For the Spray ILGAR CuInS$_2$ spectra all determined diameters of the confining spheres are smaller than the critial diameter of 2.5 nm, so that these values for L merely indicate that the actual diameter has to be smaller than this critical value. In conclusion, these considerations indicate that the uncertainties of the determined diameters L of the confining domains originating from the goodness of the fits is small compared to that arising from a possible uncertainty of the phonon dispersion relation. Therefore, the only uncertainties stated for the diameters L in this section are the standard deviations of the measurements performed on the same sample. Hence, it is of paramount importance to perform complimentary experiments in order to correlate the derived diameters L of the confining spherical domains to observed physical quantities. This is the focus of section 5.4.6 and is especially important in order to asses the influence of the simplification that the confinement is caused by *spheres* of perfect crystalline order.

In conclusion, it was shown in this section that the asymmetric peak broadening of the A$_1$-Raman mode of chalcopyrite-type CuInS$_2$ thin films (RTP, Spray ILGAR) and a single crystal can be described quantitatively as well as qualitatively by simulated Raman spectra according to the PCM formalism. From these simulations, values for the diameter of spherical domains are obtained, to which the phonons are confined. The formalism was extended such that also strains can be deduced from the spectra of the polycrystalline films, which lie in the same range as published values obtained for RTP CuInS$_2$ thin films. For the polycrystalline films, the diameter of the confining spherical domains was estimated to be below 2.5 nm for the Spray ILGAR CuInS$_2$ thin film, whilst for the RTP CuInS$_2$ thin film and for the single crystal, mean values of 7.1 ± 5.8 nm and 146.2 ± 2.1 nm was determined. For the polycrystalline films tensile strains in the range of 0.14-0.71 GPa were obtained. The nature of the crystallographic defects that cause the confinement are still to be determined, which will be the focus of section 5.4.6.

5.4.6. Correlation of Crystal Structure and Phonon Confinement

In the following, the physical relevance of the diameters of the confining spherical domains L and strains p, which were derived from the Raman spectra, are discussed. Therefore, the correlation between both quantities is assessed and the distribution of crystallographic defects as observed by TEM is compared to the values of L obtained from the simulated Raman spectra.

In Fig. 5.31, the relationship between the diameters of the confining spherical domains L and strains p, which were obtained from the fits in the previous section, is shown. The data points, for which $L < 2.5$ nm are covered by the gray-shaded area, since in their simulations, the weighting structure factor $S(q)$ did not decrease to a value of zero within the wavevector range considered in the integration in Eq. (5.18). Therefore, their physical relevance becomes more questionable as the values for L decrease. In section 5.4.5., these data points were regarded to represent a domain diameter L below a critical value of 2.5 nm. However, Fig 5.31 still indicates an increase in the tensile strain for decreasing values of the domain diameter L. Thus, it may be assumed that both quantities are correlated physically.
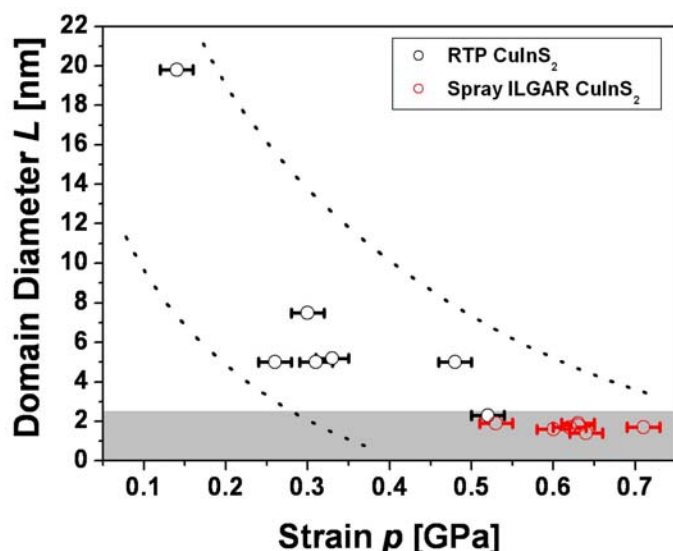

Fig. 5.31: Relation between the diameters L of the confining spherical domains and the tensile strain p, which were obtained by approximating measured Raman spectra of the A$_1$ mode of chalcopyrite-type CuInS$_2$ of a RTP-processed and a Spray ILGAR CuInS$_2$ thin film by spectra, which were simulated according to the PCM (Eq. (5.18)). The gray-shaded area marks the values, for which $L < 2.5$ nm. For these values the weighting structure factor $S(q)$ reached non-zero values outside the integration range in Eq. (5.18). The dotted lines are guides to the eye.

In order to reveal the nature of the crystallographic defects that cause the broadening of the A$_1$-mode of chalcopyrite-type CuInS$_2$, and thus assess the applicability of the PCM, TEM samples were prepared from a H$_2$S annealed Spray ILGAR CuInS$_2$ thin film and from a RTP-processed CuInS$_2$ film. Cross-sectional TEM images obtained from these films are shown in Fig. 5.32a and b. The TEM images of the Spray ILGAR CuInS$_2$ thin film (Fig. 5.32a)

revealed a high density of planar defects. These were found to be about 2-5 nm (corresponding to defect densities of 10^{19}-10^{20} cm^{-3}) apart from each other, as marked by the dashed lines in Fig. 5.32a. From the simulated Raman spectra the mean value of the confining domains was estimated to be below 2.5 nm, which is slightly below the average distance between planar defects observed in Fig. 5.32a.

In case of the RTP CuInS$_2$ film, the TEM measurements showed that the density of crystal defects differs strongly locally, even within one "grain" (Fig. 5.32b). In the region indicated by the arrow in Fig. 5.32b, the distance between neighboring planar defects is of the order of 10-20 nm (corresponding to defect densities of the order of 10^{17}-10^{18} cm^{-3}). This is about 2-3 times higher than the mean diameter of the confining domains, which was determined from the simulated Raman spectra for the RTP CuInS$_2$ thin film (Table 5.4). However, in some regions in Fig. 5.32b, no planar defects are visible (right edge of Fig. 5.32b), whereas in most parts of the grain numerous planar defects were observed. This might be partially because the visibility of planar defects depends on their orientation in the sample. It should also be taken into account that the laser spot used for the Raman measurements is of the same size as the area depicted in Fig. 5.32b. Thus, the spectrum resulting from such measurements averages over this area.
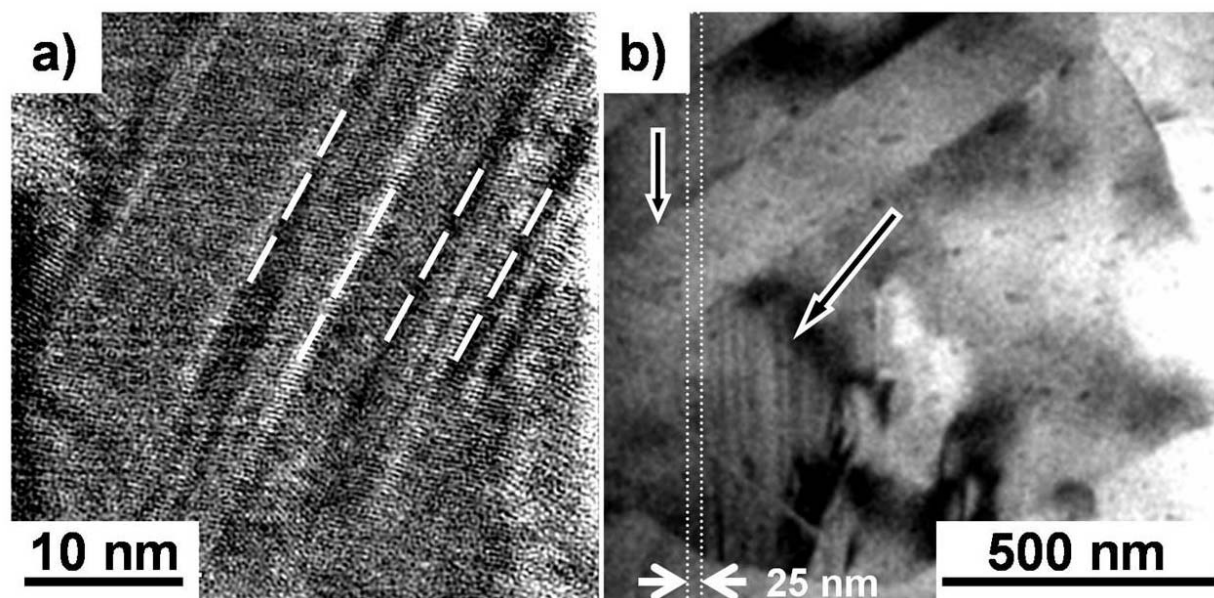

Fig. 5.32: Cross-sectional TEM images of a H$_2$S annealed Spray ILGAR CuInS$_2$ thin film (a) and of a RTP-processed CuInS$_2$ thin film (b). The location of planar defects is indicated in a) by the dashed lines. The arrow in b) indicates a region of a high density of planar defects.

From the TEM images in Fig. 5.32 it can be seen that in the Spray ILGAR and RTP-processed CuInS$_2$ thin films planar defects have typical distances of 2-5 nm (Spray ILGAR) and 10-20 nm (RTP). These distances are about 2-3 times higher, than the diameters of confining spherical domains L, which were determined from simulated Raman spectra of the A$_1$ mode of chalcopyrite-type CuInS$_2$ ($L < 2.5$ nm for Spray ILGAR CuInS$_2$; $L = 7.1 \pm 5.8$ nm for RTP CuInS$_2$ films).

However, it was already stated by Nemanich et al. [Nemanich '81], when introducing the PCM, that the width and asymmetry of their simulated Raman spectra underestimated the size of the confining domains and are therefore to be understood as a lower limit. Nemanich et al. attributed this effect to the fact, that the PCM neglects surface and domain boundary scattering effects, which may also contribute to the peak broadening. In this respect, the TEM measurements indicate that the planar defects may cause a confinement of phonons and thus lead to the asymmetric broadening.

The correlation between the diameters of the confining spherical domains L and the strains p that was indicated by Fig. 5.31, further supports the assumption that the phonon confinement is caused by the planar defects. It is known that the presence of strain can lead to the formation of planar defects in chalcopyrite-type compounds in order to reduce this strain [Couderc '86; Couderc '89; Eba '00]. Generally, the strain can be expected to exhibit a hydrostatic as well as a shear component. Since planar defects are mostly formed by a glide along the along the {112}-plane of the chalcopyrite lattice [Couderc '86; Couderc '89], only the shear component of the strain is reduced by their formation, while the hydrostatic (compressive or tensile) component remains. The latter can then influence the Raman spectra as described in section 5.4.1. Thus, a sample containing a high density of planar defects, corresponding small diameter of the confining domains in the above interpretation, would be expected to exhibit a strong residual hydrostatic strain, which leads to a shift of the Raman spectrum, as it is indicated from Fig. 5.31.

Planar defects are the most frequently observed crystallographic defects in chalcopyrite-type thin films [Li '03] and crystals [Shukri '97]. Such defects constitute planes of the crystal lattice, in which the stacking sequence of the lattice is disturbed due to the presence of the "wrong" species with respect to the original sequence, i.e. …-Cu-S-In-S-*In*-S-Cu-… instead of …-Cu-S-In-S-*Cu*-S-In-… [Holt '07]. Hence, the periodicity of the crystal lattice is broken by the planar defect. A change of the stacking sequence changes the local vibrational properties compared to those of the perfect crystal. Thus, it seems reasonable to assume that the planar defects may cause a confinement of phonons to the crystalline units of perfect crystalline order between the defects. In order to further support this assumption, it would be highly desirable to investigate the distribution of such planar defects by complimentary integral analysis techniques, such as grazing incidence XRD, in the future.

5.5.   Summary of Chapter 5

In this chapter, a comprehensive characterization of the Spray ILGAR CuInS$_2$ thin films was performed by applying Raman spectroscopy.

In section 5.2., it could be shown that the *well-crystallized top layer* and the *layered bottom layer* of the Spray ILGAR CuInS$_2$ thin films contain different amounts of CuAu-ordered CuInS$_2$ phases. Whereas the *well-crystallized top layer* solely consists of chalcopyrite-type CuInS$_2$, CuAu-ordered CuInS$_2$ was found to dominate the Raman spectrum obtained from the *layered bottom layer* of the film. This could be explained by a hindered crystallization process, which may be caused by the carbon-containing interlayers in the layered part of the film. Furthermore, a dependence of the chalcopyrite-type CuInS$_2$ $B_2{}^1{}_{LO}$ and $E^1{}_{LO}$ mode intensities on the phase purity in the probed CuInS$_2$ thin films was observed for the first time.

In section 5.3., the carbon-containing interlayers in the *layered bottom layer* were shown to consist of elemental carbon. The carbon D- and G-mode Raman signals obtained from these carbon-interlayers indicate that they contain nanocrystalline graphite and amorphous carbon.

In section 5.4., the asymmetry of the A_1-mode of chalcopyrite-type CuInS$_2$ that was observed in the Raman spectra of a Spray ILGAR and a RTP CuInS$_2$ thin film as well as of a CuInS$_2$ single crystal, could be explained by the phonon confinement model. It was shown that this model describes the observed asymmetry both qualitatively and quantitatively. Simulated spectra based on the model were correlated to the measured Raman spectra. Thereby, diameters of spherical domains were obtained, which the phonons are confined to. The comparison of these diameters with distances between planar defects in Spray ILGAR and RTP CuInS$_2$ films indicates that the planar defects may cause the phonon confinement, i.e. the observed peak asymmetry. By extending the formalism of this model, the strains present in the films could also be determined by Raman spectroscopy.